PRE-COSTAR PHOTOMETRIC CALIBRATION OF THE FAINT OBJECT SPECTROGRAPH

D. J. Lindler and R. C. Bohlin
Space Telescope Science Institute

FOS Instrument Science Report CAL/FOS-125
June 1994

ABSTRACT

The pre-COSTAR absolute photometric calibration of the Faint Object Spectrograph is derived from observations of five spectrophotometric standard stars (G191B2B, BD+75D325, HZ-44, BD+33D2642, and BD+28D4211) in the 4.3" entrance aperture for 14 detector-disperser combinations (six for the blue digicon and eight for the red). Observations of the five stars over the period of January 1991 through December 1993 show variations of the sensitivity with time. There is a systematic decline of the combined efficiency of the FOS optics and detectors, as well as a dependence of throughput on the excursions of the OTA focus from the established "best focus" position. The systematic sensitivity loss is typically 10% but is as large as 27% for the red H19 grating mode. During 1992 and 1993, the loss of sensitivity proceeded at a lower rate than in 1991.

A correction algorithm is presented that approaches an internal photometric precision of 1% in the high dispersion gratings for our ensemble mean of many calibration spectra, which implies a photometric accuracy for an individual stellar observation that is limited by the photon statistics, pointing accuracy, OTA breathing, and aperture size of the particular spectrum.

1. INTRODUCTION

Each spectrographic mode has an absolute calibration, i.e. sensitivity (S) that can be used to derive the flux of a point source as a function of wavelength by F=C/S, where F is the flux of the source and C is the observed counts per second. S can be calculated from the count rates of spectrophotometric stars with known fluxes as:

$$S=C/F \qquad (1)$$

All observations discussed in this report were obtained in the A1(4.3") entrance aperture. The aperture transmissions for point sources (Bohlin 1993, Bohlin 1994a) define calibrations for the small apertures relative to the 4.3" aperture flux calibrations that are developed in this work. During cycles 1-3, the FOS data were calibrated according to Neill, Bohlin, and Hartig (NBH, 1992), who used calibration observations in the time interval 1991.4 to 1992.0. The fundamental differences in the NBH calibration that defines the fluxes in the current HST archive and this superceding work are the corrections for changing sensitivity over time, the correction for the deviation of OTA focus from the baseline, and the switch from the IUE flux scale in the UV to a scale defined by a pure hydrogen model atmosphere flux distribution for G191B2B. (See section 3.)

The complete set of cycle 1-3 FOS calibration data is robust enough to characterize the time changes that occured during the three years of monitoring and to determine mean calibrations that are internally consistent to about 1%, especially for the more photometric high dispersion modes. The external accuracy of the absolute flux scale is limited by how well the G191B2B model predicts the actual stellar flux distribution and is estimated to be within about 3% of the truth in the UV after normalizing to visual photometry. Thus, the accuracy of absolute fluxes measured in any FOS science observation is limited by the

uncertainties in the observation itself, rather than by any deficiencies in the calibration algorithm described here. In the future, the most likely reason to update this cycle 1-3 calibration procedure would be an improved model atmosphere with the observed few percent line blanketing for G191B2B or a difference in the calibration results from additional observations of three more WD's later in cycle 4. The range in the effective temperatures of the three new pure hydrogen WD's is from 33,000 to 53,000K, while Teff of G191B2B is 60,000K.

In practice, the uncertainties in an individual observation stem from low counting statistics, from uncertain dark count subtraction, from pointing errors, from light scattered off the gratings, from thermal effects on telescope (OTA) focus i.e. "breathing", and from scatter in the positioning of the spectrum on the FOS diode array. The calibration data for the five bright calibration standard stars do not suffer from the first three of these possible errors, because of high signal levels and peak-up target acquisitions that are accurate to 0.1 arcsec in each axis. The latter three sources of photometric error are discussed in section 7.

2. FOS DATA PREPARATION

The IDL testbed version of the standard FOS pipeline reduction routine, CALFOS, is used to uniformly process all 280 individual calibration observations with the current pipeline calibration files. This standard processing includes the following steps, which produce the net count rates that are required for sensitivity computation:

1) Conversion to count rates. The raw counts are divided by the exposure time, corrected for the dead diodes, and converted to true count rates.

2) Geomagnetic image motion (GIMP) correction. Data taken before the onboard GIMP correction was implemented on 93Apr5 are shifted to correct for this problem (Fitch et al. 1993).

3) Background subtraction. A particle background and dark rate is subtracted using a background model that varies with geomagnetic latitude (Lyons et al. 1992).

4) Flat field correction. This correction uses the flat fields currently installed for use by PODPS (Anderson 1992, Lindler et al. 1993) and decouples the flat field effects from the absolute calibration procedure.

5) Residual background and scattered light is subtracted for the modes which include a wavelength region where the response to the dispersed light is zero. The scattered light correction is especially important in computing the sensitivities in wavelength regions of low sensitivity. As the sensitivity approaches zero, the scattered light becomes a large fraction of the observed light. The scattered light estimate is the average count rate in regions of zero sensitivity (Kinney and Bohlin 1993). A precise algorithm for subtraction of the FOS scattered light has not yet been developed.

6) Wavelengths are computed using the dispersion coefficient table presently used by PODPS (Kriss, Blair, and Davidsen 1991).

7) In order to monitor for possible photometric error associated with the centering of the spectra on the diode array in the direction perpendicular to the dispersion, data are collected for each observation at three different y-deflections of the diode array, one at the nominal y-position and two offset by either 0.06 arcsec or 0.12 arcsec above and below the nominal position. See

NBH and section 7 for more details. The average count rates for the lower and upper y-steps are normalized to the center y-step and averaged. NBH normalized to the y-step with the most counts; but the center y-step is the default position for GO data acquisition. The average sensitivity for the center y-step is always within 1% of the sensitivity for the maximum y-step.

3. SPECTROPHOTOMETRIC STANDARD STARS

Uncertainty in the absolute flux of the standard stars that are currently used for calibrating HST instruments and that are installed in the Calibration Database System (CDBS) is the dominant error in previous FOS absolute flux calibrations. Random photometric errors and systematic uncertainties are present in the existing reference fluxes, which are composed of IUE fluxes in the UV (Bohlin et al. 1990) and ground based spectra from Oke (1990) in the visual. Since all FOS wavelengths are measured in vacuum, the Oke wavelengths are transformed from air to vacuum values. Photometric errors are typically a few percent and range up to 10% in the difficult region for both IUE and Oke around 3200A, while the absolute IUE scale is low by 5-10% in the UV in comparison to models for pure hydrogen white dwarfs (WD). The five spectrophotometric standard stars, G191B2B (WD0501+527), BD+75D325, HZ-44, BD+33D2642, and BD+28D4211 are used for the sensitivity calibration of the FOS and have FOS spectra covering the wavelength range 1140-8500A. The differences between the FOS absolute photometry for the average spectra of these five stars and Landolt(1992) B and V photometry show an rms scatter of only ~0.5% (Colina and Bohlin 1994).

To produce proper reference star fluxes on the WD scale with 1% photometric precision, a bootstrapping procedure is necessary and is summarized by the the following steps. See Bohlin (1994b, in preparation) for more details. Since the FOS data have a higher signal-to-noise ratio (S/N) and are more photometric than IUE, the IUE data for the five standards are replaced by the FOS fluxes from a preliminary FOS calibration on an approximate WD scale. In the optical, the Oke spectra are retained, because a five meter telescope produces higher S/N spectra than FOS.

a) Adjust the Oke spectra by the mean offset of the B and V Landolt photometry (Colina and Bohlin 1994). All five stars have the 0.04 mag correction recommended in the Oke paper. Only BD+33D2642 at 0.047 mag requires an additional correction bigger than 0.01 mag.

b) Correct the Oke spectra to FOS high dispersion spectra on the red side with a smooth (10 spline node) fit to their ratio from 3300 to 8500A. Longward of 3850A, these adjustments are typically 1-2% and exceed 3% only for HZ44 longward of 8100A.

c) Form complete spectra from the following best available pieces of data:
1140-2100 FOS blue side high dispersion H13 and H19 data
2100-3300 FOS red side high dispersion H19, H27, and H40 data
3300-3850 FOS blue side high dispersion H40 data
3850-8500 Oke data corrected as in step b
>8500 Oke data corrected with the correction value at 8500A from step b.
The FOS spectra are rebinned every four sample points to reduce noise and data volume. The result of this step is a set of spectra with a relative photometry accuracy among the five standards of ~1%, so that all five should have the same correction to the WD scale per step d.

d) Correct to the WD scale by the ratio of the composite spectrum of G191B2B from step c to the pure hydrogen model for Teff=60,000K and log g=7.5 from D. Finley. The model flux is adjusted to the absolute flux level of Landolt V photometry (Colina and Bohlin 1994). All five stars are divided by the fit to the ratio, which does not exceed ~2% longward of 1200A.

The composite spectra from this procedure for BD+75D325, HZ-44, BD+33D2642, and BD+28D4211 plus the model for G191B2B are the standard star reference spectra used to produce the FOS calibrations. The remainder of HST standard star flux distributions in the CDBS will be corrected also to the WD flux scale.

4. SENSITIVITY COMPUTATION

A raw sensitivity curve is computed for each observation by taking the ratio of the processed count rate divided by the star's reference flux distribution for each of the 264 individual observations after 1991.0 as summarized by star and FOS mode in Table 1. For all dispersers except the prism, the observed FOS count rate and the reference flux distribution are rebinned using trapezoidal integration to a common wavelength scale with 5A bins or 6 FOS pixels, if 6 px is greater than 5A. For the prism, the standard star spectrum is rebinned using trapezoidal integration over the four pixel FOS diode width.

TABLE 1
NUMBER OF OBSERVATIONS FOR EACH STAR AND FOS DISPERSION MODE IN 4.3" APERTURE

Detector	Disperser	G191B2B	BD+28D4211	BD+75D325	BD+33D2642	HZ44	TOTAL
BLUE	H13 (G130H)	5	6	5	2	3	21
BLUE	H19 (G190H)	5	7	5	2	3	22
BLUE	H27 (G270H)	5	6	5	2	3	21
BLUE	H40 (G400H)	5	3	5	2	3	18
BLUE	L15 (G160L)	5	6	5	2	3	21
BLUE	PRISM	5	4	1	2	3	15
RED	H19 (G190H)	9	10	3	1	1	24
RED	H27 (G270H)	9	9	3	1	1	23
RED	H40 (G400H)	5	7	3	1	2	18
RED	H57 (G570H)	5	5	3	1	2	16
RED	H78 (G780H)	3	2	3	1	2	11
RED	L15 (G160L)	9	8	3	1	1	22
RED	L65 (G650L)	5	7	3	1	2	18
RED	PRISM	5	6	*	1	2	14

* BD+75D325 is too bright for the prism.

A least squares cubic spline is fit to the raw sensitivity curves to generate a smooth sensitivity curve. Regions on either the blue or the red digicon with large photocathode blemishes that have not been removed by flat fielding and regions on both detectors with spectral lines that are not adequately represented in the standard star reference fluxes are not used in the fitting process. These regions are listed in Table 2.

TABLE 2
REGIONS EXCLUDED FROM THE SENSITIVITY COMPUTATION

Wavelength Region (Angstroms)	Dispersive mode or star
1390 - 1435	G191B2B
1545 - 1555	G191B2B
2790 - 2810	G191B2B
3950 - 4000	G191B2B
4075 - 4125	G191B2B
4310 - 4370	G191B2B
4810 - 4910	G191B2B
6500 - 6620	G191B2B
1200 - 1232	All stars
2114 - 2135	Blue H19
2985 - 3010	Blue H27
4800 - 4930	Red H57
8300 - 8400	Red H78

A typical least squares spline fit is shown in Figure 1. The number of spline nodes used in each disperser mode is given in Table 3. An asterisk indicates that unequally spaced nodes are used. In these cases, nodes are placed at specific wavelengths to follow better the curvature of the sensitivity function.

TABLE 3
FOS MODES AND NUMBER OF SPLINE NODES

Detector	Disperser	Nodes	WL Range (A)
BLUE	H13 (G130H)	18 *	1140 - 1606
BLUE	H19 (G190H)	21 *	1573 - 2330
BLUE	H27 (G270H)	17	2221 - 3301
BLUE	H40 (G400H)	16	3240 - 4822
BLUE	L15 (G160L)	28 *	1140 - 2508
BLUE	PRISM	31 *	1500 - 5959
RED	H19 (G190H)	21 *	1590 - 2312
RED	H27 (G270H)	17	2222 - 3277
RED	H40 (G400H)	16	3235 - 4781
RED	H57 (G570H)	15	4569 - 6818
RED	H78 (G780H)	13	6269 - 8499
RED	L15 (G160L)	25 *	1571 - 2424
RED	L65 (G650L)	23 *	3540 - 7075
RED	PRISM	28 *	1620 - 8887

Each raw sensitivity curve is corrected for throughput variations resulting from changes of the OTA focus due to desorption (Lindler & Bohlin 1993, Hasan 1994). These sensitivity curves are averaged for each mode and are shown in Figure 2. Data taken prior to 91Jan1 are not included in the averages because of large uncertainties of the focus correction for that time period.

In the case of L15 blue, the wavelength range in Table 3 is more than a factor of two, so that there is contamination of the first order longward of ~2300A by second order light. Quantitative estimates of this problem are provided by FOS sky spectra, which have a count rate due to second order Lyman-alpha of about one-half of the first order count rate. For a continuum source, the doubling of the dispersion in second order causes a drop in the relative contamination by another factor of two. The relative sensitivity to a continuum source at 1216A vs. 2432A is a factor of 48, so that for a flat continuum source (F(lambda)=constant), the first order light contamination at 2432A is only ~0.5% and has been ignored in the L15 calibration results.

5. TIME VARIATIONS OF THE SENSITIVITY.

Changes of the FOS sensitivity over time are measured by the ratio of the focus-corrected individual sensitivity curves to the average sensitivity curve for each dispersion mode. Both denominator and numerator of these ratios are represented by the spline fits to avoid noise spikes that could dominate the ratio. The ratios are then averaged over different wavelength bins and displayed in Figures 3-4. The following wavelength bins are used:

Three equal wavelength bins:
RED: H40, H57, H78, L65
BLUE: H13, H19, H27, H40, L15

Three unequal wavelength bins with the specified wavelength limits:
RED Prism: 2500, 2950, 3899, 8000 Angstroms
BLUE Prism: 2000, 2318, 2973, 5500 Angstroms

Red H19: 1590 to 1630, 1630 to 1660, and 10 Angstrom bins for the remaining spectral coverage.

Red H27: 20 Angstrom bins

Red L15: 1570 to 1720, 1720 to 1750, and 10 Angstrom bins for the remaining spectral coverage.

The changes of FOS sensitivity are independent of wavelength for the six blue side modes plus the red side H40, H57, H78, L65, and prism modes. These changes are displayed in Figure 3, where different symbols are used for observations from different stars. The symbols are connected by different line types for each of three wavelength regions. The three line types track the mean fit well and justify the wavelength independent solution for the change of sensitivity with time. The blue side sensitivity decreased rapidly until 1991.7 for all disperser modes. After that date, the rate of change slowed. The blue side time changes are modeled by a two straight lines connected at 1991.7 (heavy solid lines). These least square fits are computed using the average of the three wavelength bins. An exponential fit models the time variations on the red side. Since little sensitivity monitoring was done in 1990, a flat model at the 1991.0 value is shown for the few observations that exist in 1990.

Since the time change of sensitivity is a function of wavelength for the red H19, H27, and L15 modes, a separate exponential model is computed for each wavelength bin. The bin size quoted above is the minimum width required to track the changes with sufficient accuracy to use linear interpolation for intermediate wavelengths. Figure 4 shows the fits for the wavelength bins with the maximum rate of change for H19, H27, and L15. These sets of models for the red H19, H27, and L15 modes are evaluated at 6 month intervals and plotted versus wavelength in Figure 5a-c.

6. RESULTS

Figure 6 shows the FOS blue and red side spectra for G191B2B that result from co-addition of individual observations after calibration by the above procedure. Also shown for comparison are the pure hydrogen model for G191B2B that is used for the fundamental absolute flux reference, the composite standard star spectrum that results from the steps a-d in section 3, and the original CDBS composite standard star spectrum that consists of IUE data plus Oke spectrophotometry. All of these fluxes are scaled by wavelength to the 3.5 power, in order to illustrate features at the 1-10% level. The 10% dips at 1400 and 1640A in the SWP IUE data and the poor quality of the IUE long wavelength data are evident in the CDBS spectrum, which can now be replaced in the STScI Calibration Data Base by the improved standard star composite spectrum.

7. ERROR ANALYSIS

7.1 Internal Consistency of FOS Modes

Figure 7 is the check on the internal consistency of the calibration procedure. The final calibrated fluxes for each star are co-added and compared to the input standard star spectrum, which is the model in the case of G191B2B. For each star, six panels in Figure 7 show the ratio of the FOS output fluxes over the standard star input flux for all of the high and low dispersion modes. Except for occasional blips that are caused by mismatches in spectral resolution or by partially corrected flat field features, the residuals are generally less than ~2% for the high dispersion gratings. The spike at 8300-8400A and excess scatter longward of 6300A is a caused by the lack of any flat field correction for H78. Selected broadband averages of the residual deviation from unity are shown in each panel and do not exceed 0.4% in any high dispersion case, except for one part of the HZ44 spectrum that has only two observations. Thus, these results demonstrate a precision of ~1% in our high dispersion calibrations, which are smooth spline fits that are unaffected by blips. For the prism, longward of ~4000A on the blue side and ~5000A on the red side, small shifts of 1-2px on the diode array cause significant photometric errors as shown in Figure 8. Similar problems afflict the low dispersion red side gratings L15 and L65 in the regions of their steep short wavelength cutoffs. The photometry for BD+33D2642 shortward of 1640A on L15 and shortward of 3850A on L65 are especially bad, since there is only one red side spectrum with no chance for the shifts to average out.

An example of one of the worst cases of internal consistency in high dispersion appears in Figure 9 as a difference of 2.4% in the G191B2B fluxes from H13 and H19 blue. This difference of 2.4% is ~3 sigma, calculated from the difference of two observations, each of which are the average of 5 observations each with the one sigma uncertainty of 1.2-1.4% from Table 4. However, the ends of the spectra are less photometric, because distortion in the Digicon causes curvature of the spectrum at the diode array. Thus, the offset shown in Figure 9 is probably more on the order of a two sigma deviation.

7.2 Changes of the External Absolute Flux Reference Standards

How do the fluxes from this FOS calibration differ from the archival fluxes that are based on the NBH calibration? The FOS flux calibration specified by NBH went into the routine pipeline processing on 92-Apr-1 at 17:39 and has been used for all subsequent processing and reprocessing that has produced a uniform archive of cycle 1-3 FOS fluxes. The changing sensitivity complicates the comparison between these archival NBH fluxes and our new time dependent calibration, which is on the WD scale. Figure 10 shows the ratio of these two calibrations for an early and a late observation, which span the time range in question. Figure 10a shows this ratio for actual old pipeline reductions, while 10b corrects the old NBH fluxes for the focus of the OTA (Lindler & Bohlin 1993). This focus correction amounts to almost 5% on 1991.0, since the desorption had moved the focus to -14 microns from nominal. Thus, Figure 10b isolates changes of flux to just the combined effects of changing FOS sensitivity and the new WD absolute flux scale.

7.3 Uncertainty of the Photometry of Single Observations

Section 7.1 discusses the repeatability of FOS for co-adds of multiple observations, while the typical Guest Observer is more concerned with the uncertainty associated with single observations. The last column of Table 4 contains the one sigma rms scatter for the points defined by the wavelength bins of section 5 with respect to the fits shown as heavy solid lines for the time change in sensitivity displayed in Figures 3-4. Both the correction for the focus error of the OTA and the correction for the systematically changing sensitivity with time are reflected in the last column labeled Focus-Time, while the column No Focus-No Time is the scatter about the average sensitivity without correction for either effect. Our correction procedure reduces the scatter by a factor of 2-3. The high dispersion gratings, excluding H19 Red, have an average sigma of 1.1% and are better photometers than the low dispersion gratings, while sigma for the prisms is 2.6%. The residual 1-2% scatter may be attributed to the short term effects of OTA "breathing" caused by thermal changes during an orbital period (Hasan & Bely 1993). However, no accurate model for throughput variations due to "breathing" can be implemented with the engineering data currently available to the RSDP. In cycle 4, the smaller PSF should reduce the sensitivity to the effects of breathing and lower the scatter. Absent any pointing error and with sufficient counting statistics, the broadband photometric performance of FOS is summarized without and with our corrections in the last two columns of Table 4, respectively.

TABLE 4
ONE SIGMA BROADBAND PHOTOMETRIC SCATTER OF SINGLE OBSERVATIONS IN PERCENT

		No Focus No Time	Focus Time
BLUE	H13	4.2	1.2
BLUE	H19	4.5	1.4
BLUE	H27	3.3	0.8
BLUE	H40	3.4	1.4
BLUE	L15	4.8	1.5
BLUE	PRI	4.3	2.5
		---	---
AVERAGE		4.1	1.5
RED	H19	5.4	1.7
RED	H27	2.9	1.2
RED	H40	3.2	1.1
RED	H57	2.9	1.1
RED	H78	2.3	0.9
RED	L15	5.0	2.5
RED	L65	3.6	2.0
RED	PRI	3.2	2.7
		---	---
AVERAGE		3.6	1.7

7.4 So Why do Some Observations Occasionally produce Lousy Photometry?

The susceptibility of the Digicons to the geomagnetic field (GIMP) causes image motion up to ~0.2 arcsec from the mean (Fitch et al. 1993). The onboard correction for GIMP began on 1993.26 (93-Apr-5). Since Figures 3-4 demonstrate good photometry both before and after that date, other problems must contribute to cases of bad photometry.

Photometric error can be caused by errors in the placement of the target in the direction perpendicular to the spectral dispersion (y). For the A1(4.3") aperture, an error of 0.7 arcsec places the target on the edge of the diode array and causes a loss of 50% of the expected signal. Smaller aperture may show even larger photometric errors than those discussed in this paragraph for the A1(4.3") aperture . Contributing factors to these y position errors are GIMP, tolerance in the internal FOS mechanisms, and imprecision in providing the best average ybase position for the spectra at any given time. The history of the ybase positions measured by the internal FOS lamp are provided by Koratkar and Taylor (1993) and by Koratkar et al. (1994). Since 1991.86 for the four most used high dispersion gratings on each side, these internal errors are summarized in Table 5, which indicates that large blue side errors are more frequent than on the red side. For example, 11 of the 46 measured blue side y positions are more than 0.2 arcsec from the commanded ybase position, while one blue side error is 0.44 arcsec. Evidently, errors of this magnitude in conjunction with the precision target acquistions of <0.1 arcsec y-error in the observations of the five standard stars do not cause photometric errors beyond those summarized in Table 4. However, pointing errors in y of only ~0.3 arcsec cause serious photometric losses with a rather high frequency, especially on the blue side. Even a 0.2 arcsec error in y, which is typical of many GO target acquisition strategies, will cause big photometric errors some fraction of 1% of the time, if the 0.44 arcsec error in one case out of 92 is a typical frequency.

TABLE 5
INTERNAL FOS YBASE ERROR FREQUENCY

Detector	>0.2 arcsec	>0.3 arcsec	>0.4 arcsec	Total Cases
Blue	11	3	1	46
Red	3	1	0	46

For programs with precise photometric requirements, a precise acquisition strategy and a confirming post-acquisition FOS image of the 4.3 arcsec aperture (Vassiliadis et al. 1994) is recommended. Post-COSTAR photometry is expected to improve because of the smaller PSF, fixing of the GIMP on 1993.26, and better tracking of the average commanded ybases. Binary target acquisition errors may also decrease.

For short observations, jitter can carry the target out of the aperture and cause a significant loss of signal. Only one (Y0K40408T) of the 264 calibration observations showed >5% photometric error at all wavelengths; and that short integration of 18 sec/y-step is ~10% low, probably because jitter carried the star off the diode array. One signature of jitter is systematic differences among the mean countrate of the four x-steps.

8. SUMMARY

Recipe for final flux calculation for point sources:

1) Correct the net count rates for the aperture throughput relative to the A1(4.3") aperture from Bohlin (1994a).

2) Compute the focus position from the observation time using the focus history, and correct the count rates to the zero OTA focus position per Lindler & Bohlin (1993).

3) Convert count rates to fluxes according to Eq. 1 by using the average sensitivities for the A1(4.3") aperture.

4) Correct the fluxes for the sensitivity change with time from according to the fits depicted in Figures 3-4.

This algorithm is being coded into the STSDAS version of CALFOS and should be available for public use in reprocessing cycle 1-3 FOS observations later this year. Currently, there are no plans for complete reprocessing of archival data.

The reference files and tables for this calibration algorithm will be available on STEIS/MOSAIC and from the STScI data archive.

REFERENCES

Anderson, S. F. 1992, FOS Instrument Science Report CAL/FOS-075.

Bohlin, R. C. 1993, FOS Instrument Science Report CAL/FOS-106.

Bohlin, R. C. 1994a, FOS Instrument Science Report CAL/FOS-120.

Bohlin, R. C. 1994b, in preparation.

Bohlin, R. C., Harris, A. W., Holm, A. V., & Gry, C. 1990, ApJS., 73, 413

Colina, L., & Bohlin, R. C. 1994, AJ, submitted.

Finley, D. 1994, private communication.

Fitch, J., Hartig, G., Beaver, E. A., & Hier, R. 1993, FOS Instrument Science Report CAL/FOS-098.

Hasan, H. 1994, OTA Instrument Science Report OTA-16.

Hasan, H., and Bely, P. 1993, BAAS, 25, 1460.

Kinney, A. L., & Bohlin, R. C. 1993, FOS Instrument Science Report CAL/FOS-103.

Koratkar, A., & Taylor, C. 1993, FOS Instrument Science Report CAL/FOS-116.

Koratkar, A., Taylor, C., Kinney, A., & Keyes, C. 1994, FOS Instrument Science Report CAL/FOS-116.

Kriss, G., Blair, W., & Davidsen, A. 1991, FOS Instrument Science Report CAL/FOS-067.

Lyons, R., Baity, W., Beaver, E., Cohen, R., Junkkarinen, J., Linsky, J., & Rosenblatt, E. 1992, FOS Instrument Science Report CAL/FOS-080.

Landolt, A. 1992, AJ, 104, 340.

Lindler, D. J., & Bohlin, R. C. 1993, FOS Instrument Science Report CAL/FOS-102.

Lindler, D., Bohlin, R., Hartig, G., & Keyes, C. 1993, FOS Instrument Science Report CAL/FOS-088.

Neill, J. D., Bohlin, R. C., & Hartig, G. 1992, FOS Instrument Science Report CAL/FOS-077 (NBH).

Oke, J. B. 1990, AJ, 99, 1621.

Vassiliadis, E., Bohlin, R., Koratkar, A., and Evans, I. 1994, FOS Instrument Science Report CAL/FOS-122.

FIGURE CAPTIONS

Fig. 1-Typical least square spline fit to the sensitivity for one observation in the upper panel and the residuals in the lower panel.

Fig. 2-Average sensitivity curves reduced to nominal OTA focus=0 for the 1991-1993 period in the (a) high dispersion modes and (b) low dispersion modes. Solid lines are the blue side sensitivities, while dashed lines represent the red side results.

Fig. 3-Change of sensitivity with respect to the averages of Figure 2 for the FOS modes with no dependence on wavelength. The data for three broad wavelength bins are shown and are connected by different line types. The heavy solid line is the adopted fit.

Fig. 4-Examples of sensitivity change for the three red side modes that are afflicted with a wavelength dependence. Bin sizes are 10A for H19 and L15, while 20A bins are sufficient for H27. The three independent exponential fits are heavy lines of the same type that connect the individual data points.

Fig. 5-Corrections as a function of wavelength for the three modes of Figure 4 evaluated at six month intervals. Figure 5a shows a maximum drop in sensitivity from 1991.0 to 1994.0 of 0.91/1.24=0.73 at 1975A for H19.

Fig. 6-Fluxes scaled by the 3.5 power of wavelength for G191B2B from the top: a pure hydrogen model atmosphere (Finley 1994), which is the primary standard candle for the FOS calibration, the composite data used for the standard star spectrum, the complete FOS red side high dispersion spectrum, the FOS high dispersion spectrum from the blue side, and the original standard star spectrum, which illustrates problems at the ~10% level. The original fluxes have the infamous IUE bumps and dips, bad S/N in the IUE 2000-3200A region, and smaller shape problems with the ground based Oke data; but the FOS results of our new calibration do not exhibit these problems.

Fig. 7-Residual ratios of the co-added spectrum of each star divided by the input standard star spectrum for (a) G191B2B, (b) BD+28D4211, (c) BD+75D325, (d) BD+33D2642, and (e) HZ44. The pure hydrogen WD spectrum is the standard star for G191B2B. The six panels in each plot are blue-red pairs of high dispersion gratings, low dispersion gratings, and prism modes, respectively. Selected broadband averages of the residuals are shown in each panel

Fig. 8-Photometric effect of 1-2 pixel (=0.25-0.5 diode resolution element) shifts in the position of the spectrum on the Digicon detectors. The solid and dashed lines are the one and two pixel shifts, respectively, and represent the range of expected stability for the blue (upper panel) and red (lower panel) sides.

Fig. 9-A worst case difference in the overlap fluxes for the standard G191B2B. The offset of 2.4% between the H13 and H19 results can be understood in terms of the statistics of the photometric repeatability of the FOS.

Fig.10a-Ratio of archival fluxes on NBH scale to those obtained using the correction technique and WD scale specified here. High dispersion data is shown for the blue (solid line) and red (dotted line) side on 1991.0 (upper panel) and on 1993.7 (lower panel.) Most of the blue side features correspond to the WD correction and can be seen in Figure 6, also. Longward of 3900A, the structure in the ratio is due to improvements in the treatment of the Balmer lines as described in section 4 and Table 4. The general loss of sensitivity in all modes is shown by smaller ratios in the lower panel compared to the upper panel. The rapid loss of sensitivity in H19 red near 2000A appears as the biggest change from upper to lower panel.

Fig.10b-Same as 10a, except that the old archival fluxes are corrected for OTA focus changes in order to isolate the effects of the time changes and the WD flux scale change from the OTA focus errors.

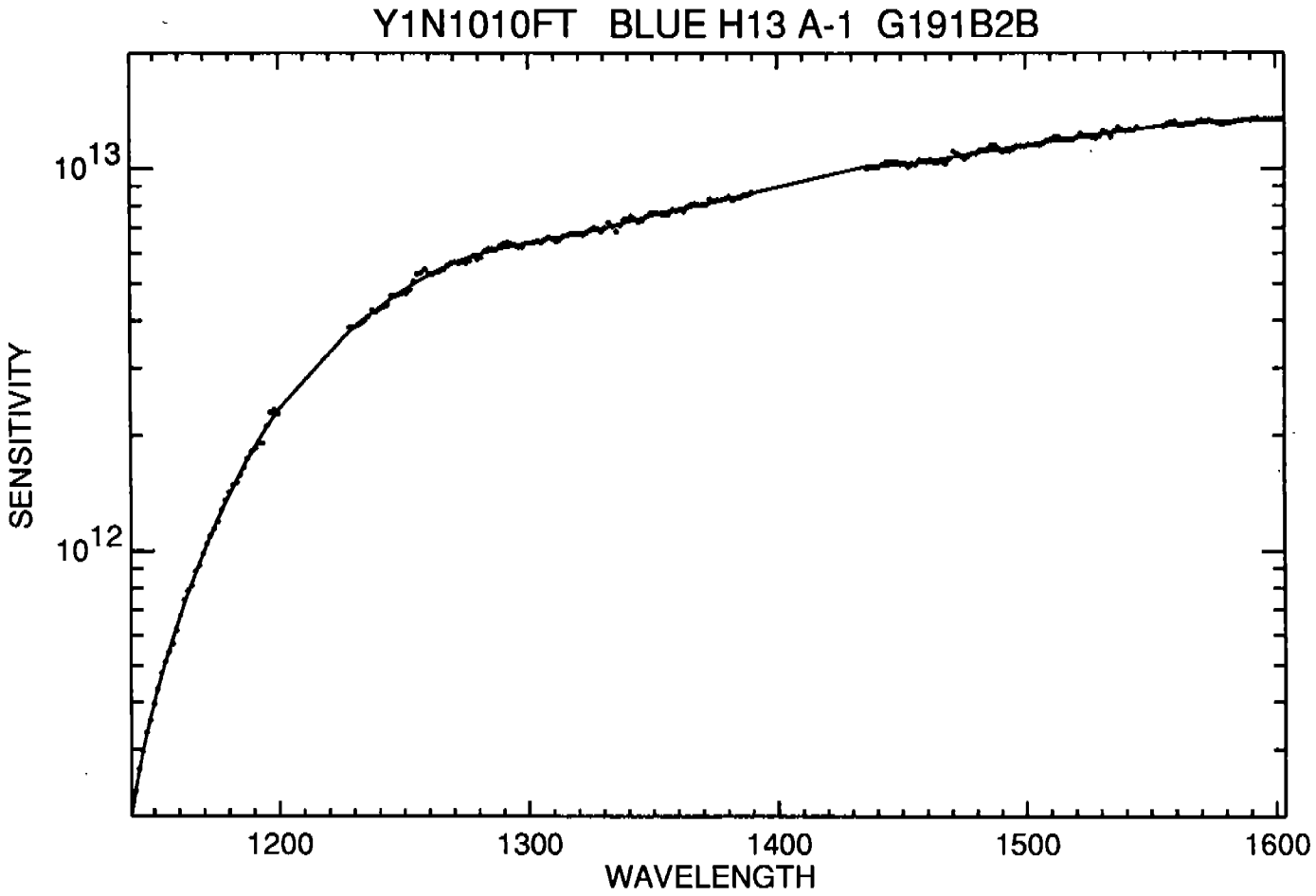
Y1N1010FT BLUE H13 A-1 G191B2B
SENSITIVITY
10^{13}
10^{12}
1200
1300
1400
1500
1600
WAVELENGTH

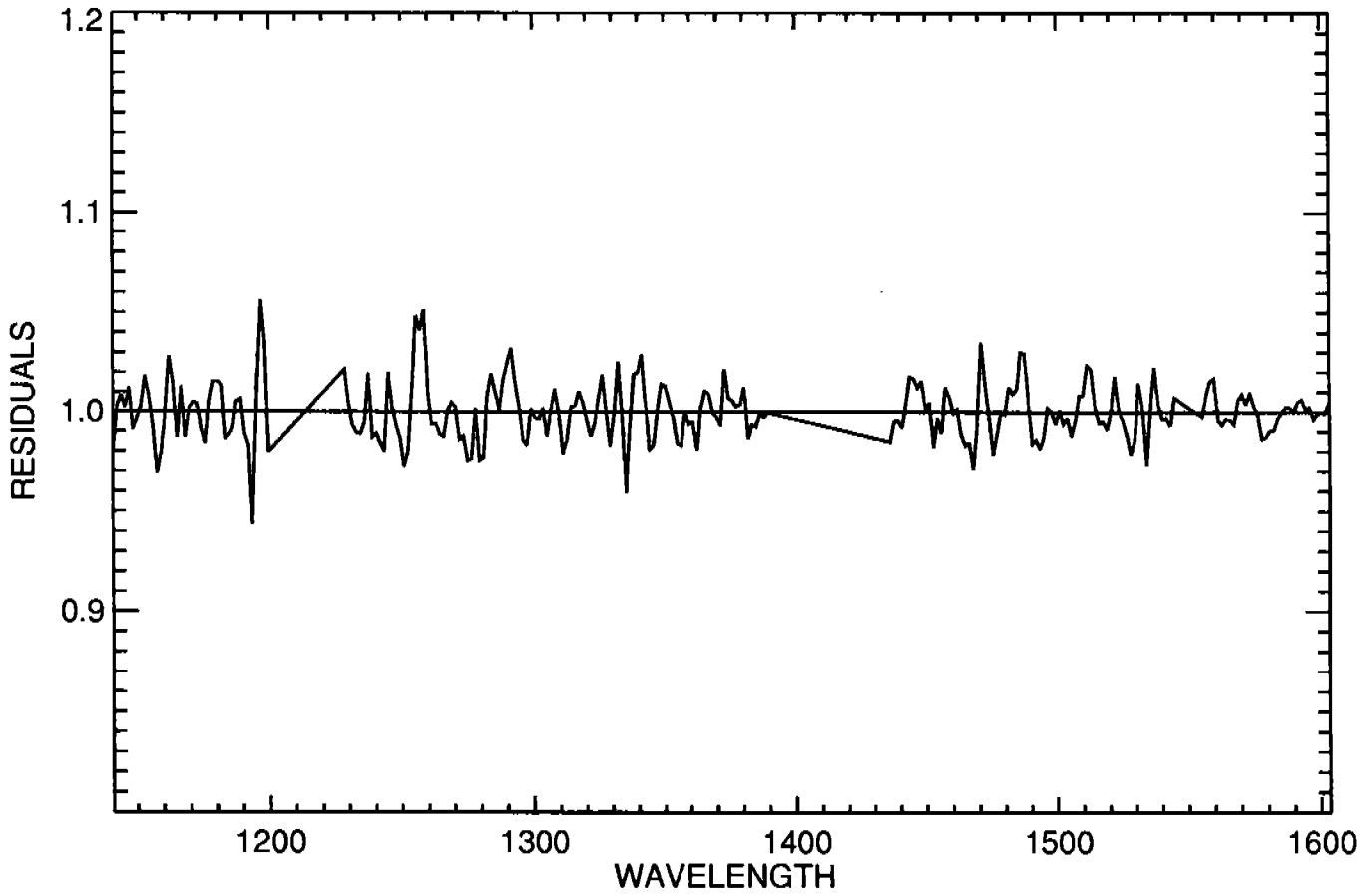
RESIDUALS
1.2
1.1
1.0
0.9
1200
1300
1400
1500
1600
WAVELENGTH

Fig. 1

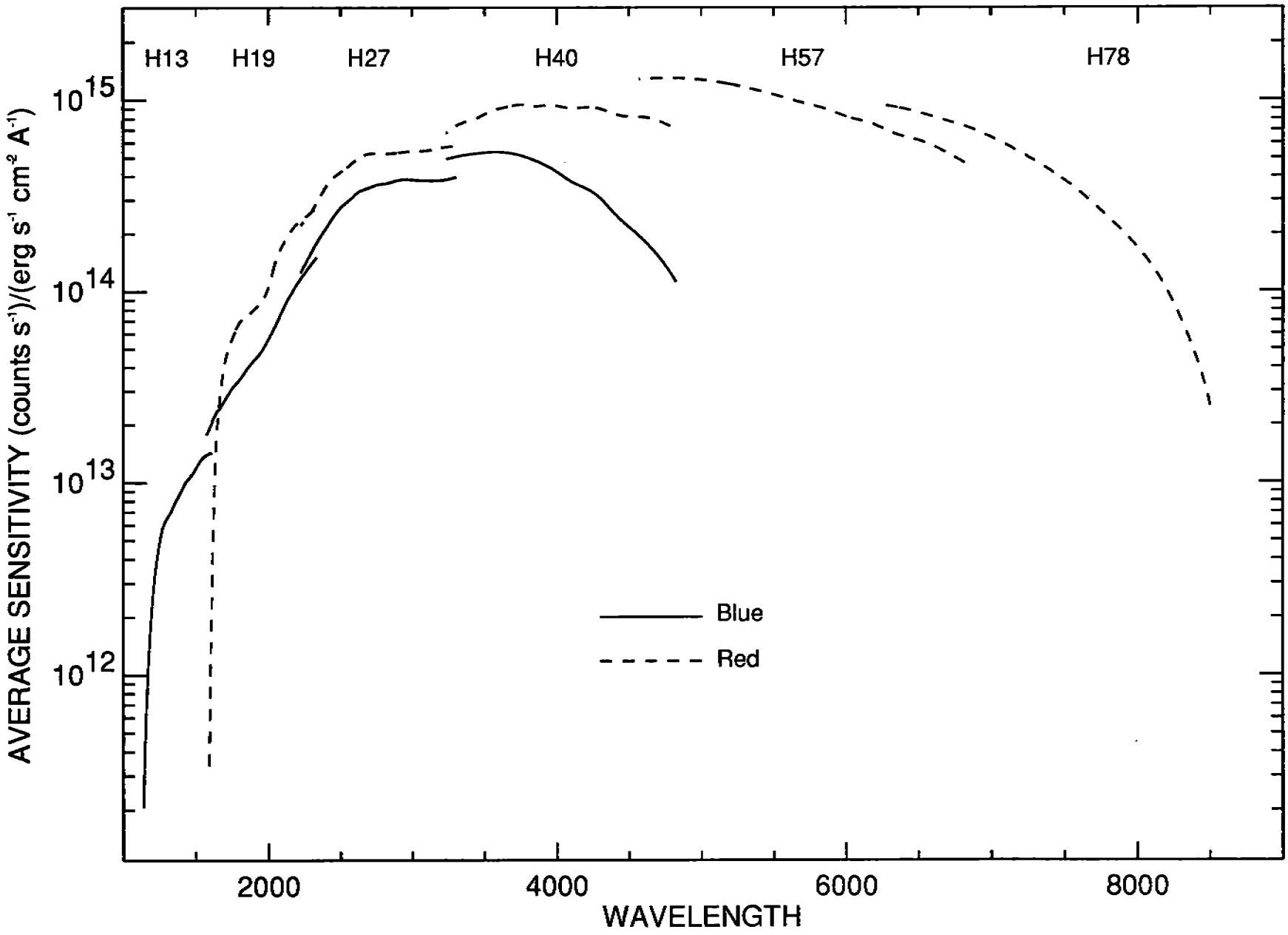
H13
H19
H27
H40
H57
H78
AVERAGE SENSITIVITY (counts s-1)/(erg s-1 cm-2 A-1)
10^15
10^14
10^13
10^12
Blue
Red
2000
4000
6000
8000
WAVELENGTH

Fig. 2a

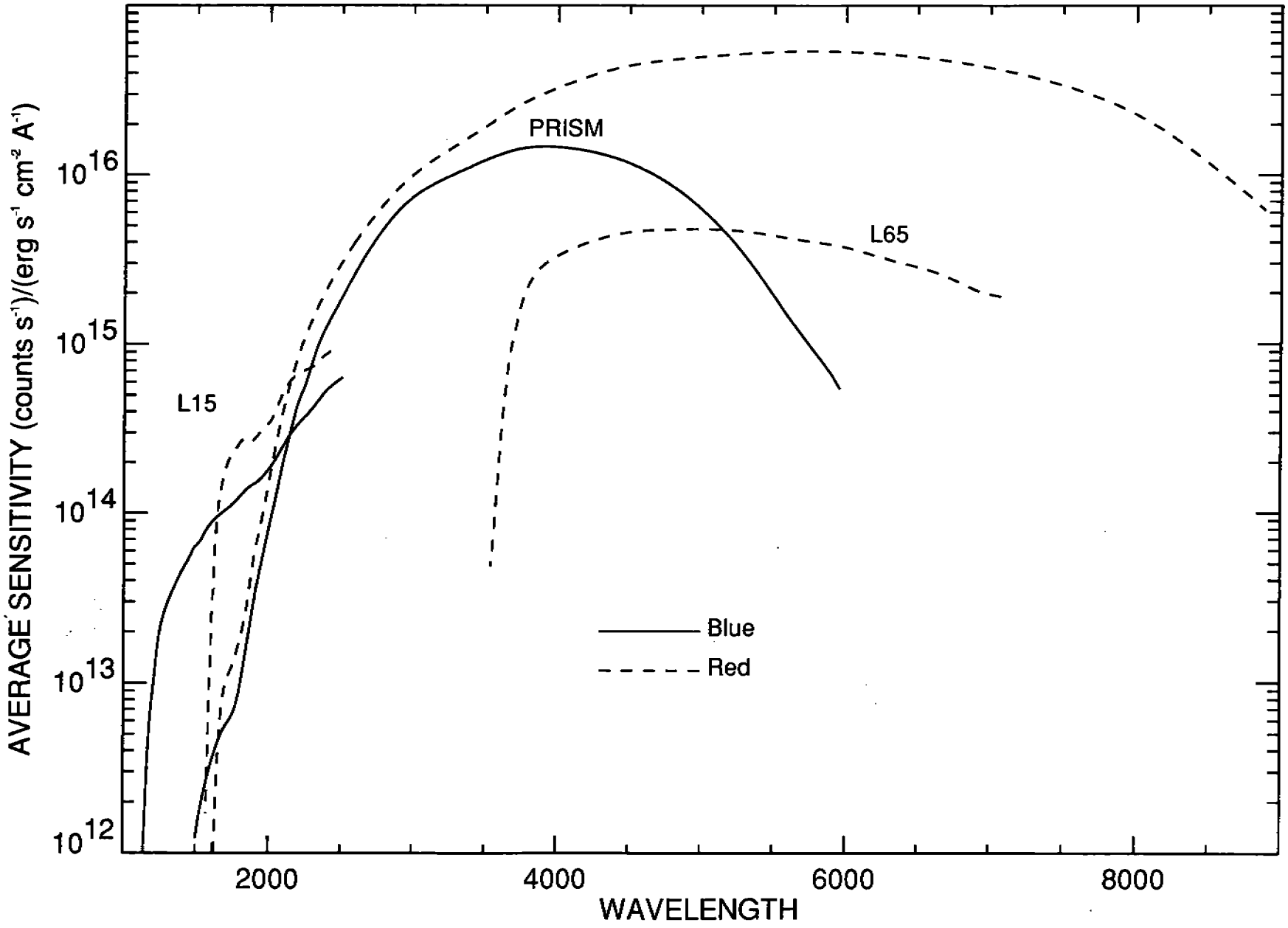
AVERAGE SENSITIVITY (counts s^{-1})/(erg s^{-1} cm^{-2} A^{-1})
10^{16}
10^{15}
10^{14}
10^{13}
10^{12}
PRISM
L65
L15
Blue
Red
2000
4000
6000
8000
WAVELENGTH

Fig. 2b

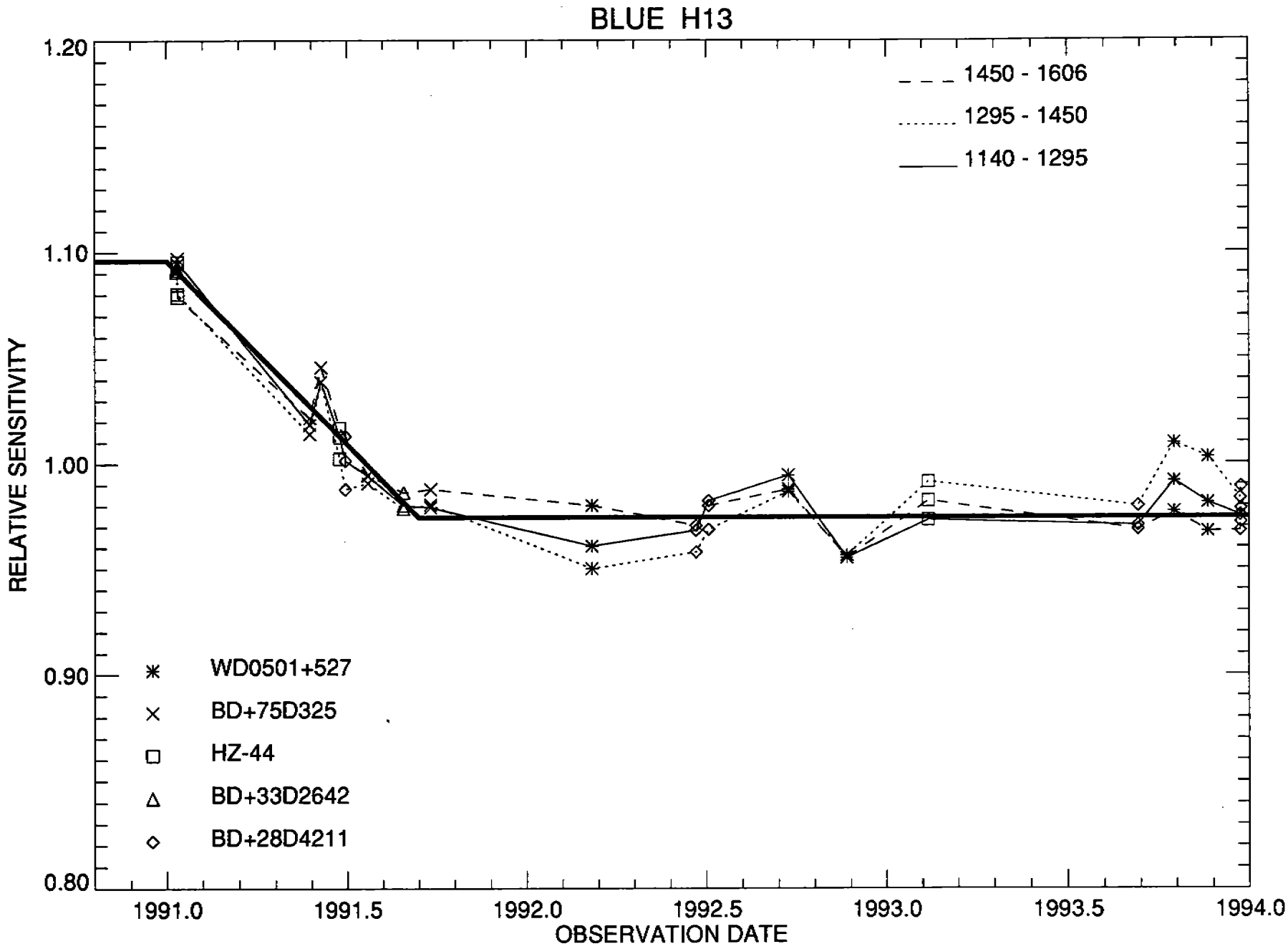
BLUE H13
1.20
1.10
1.00
0.90
0.80
RELATIVE SENSITIVITY
1450 - 1606
1295 - 1450
1140 - 1295
WD0501+527
BD+75D325
HZ-44
BD+33D2642
BD+28D4211
1991.0
1991.5
1992.0
1992.5
1993.0
1993.5
1994.0
OBSERVATION DATE

Fig. 3

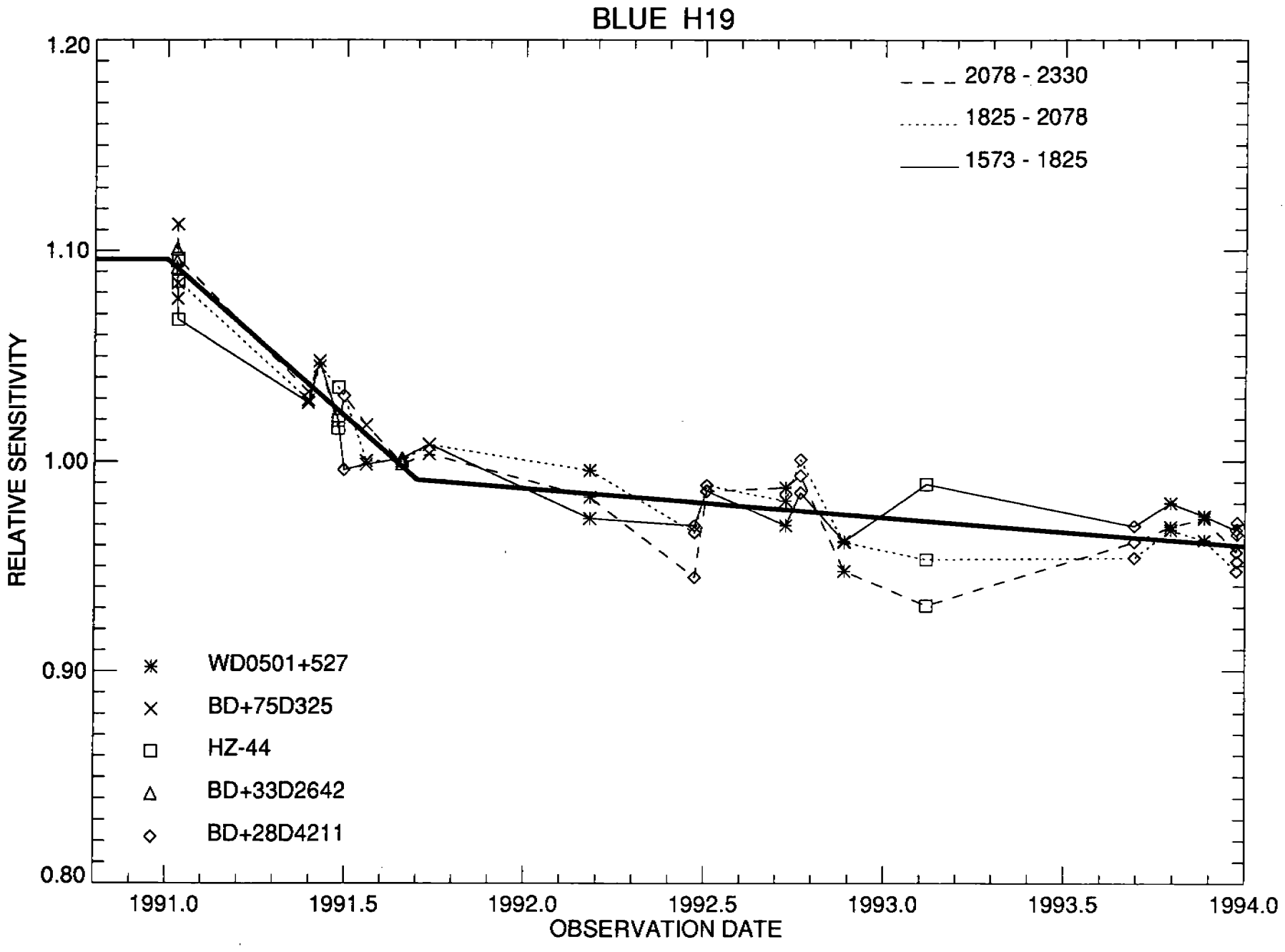

PLTSENS_TIME 11-May-1994 08:20

Fig. 3 (cont.)

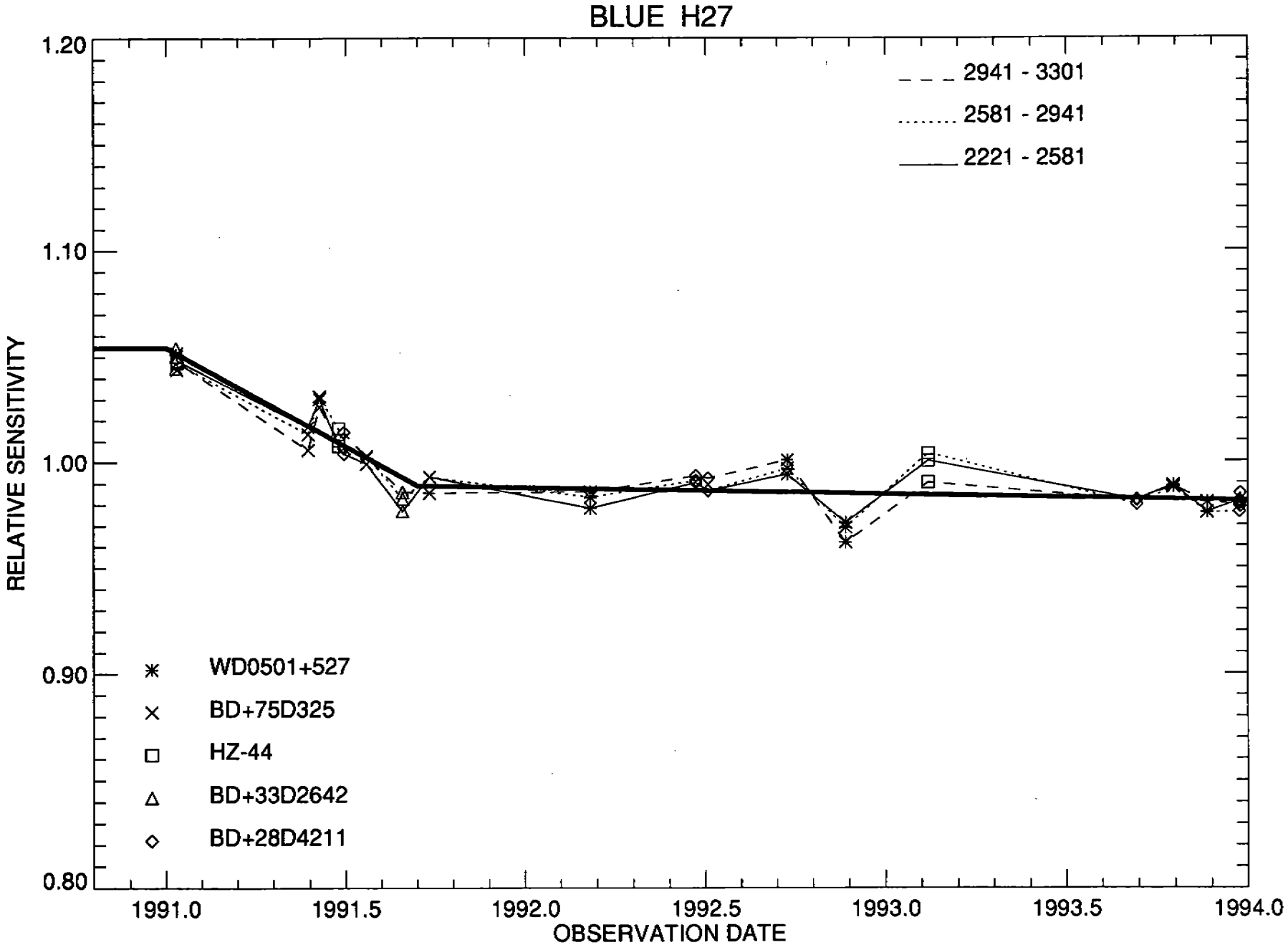

TIME 11-May-1994 06:27

Fig. 3(c

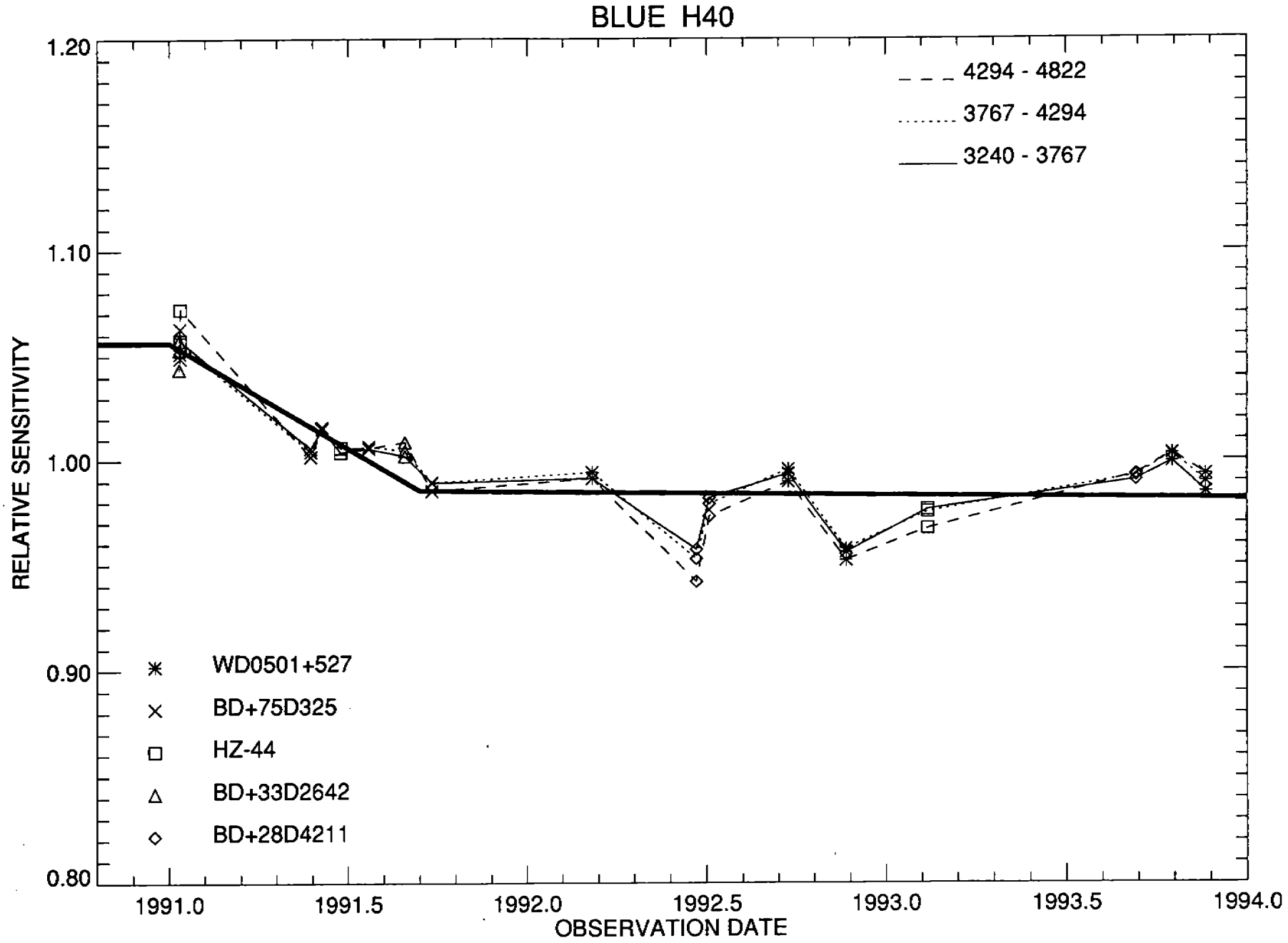

PLTSENS_TIME 11-May-1994 06:21

Fig. 3 (cont.)

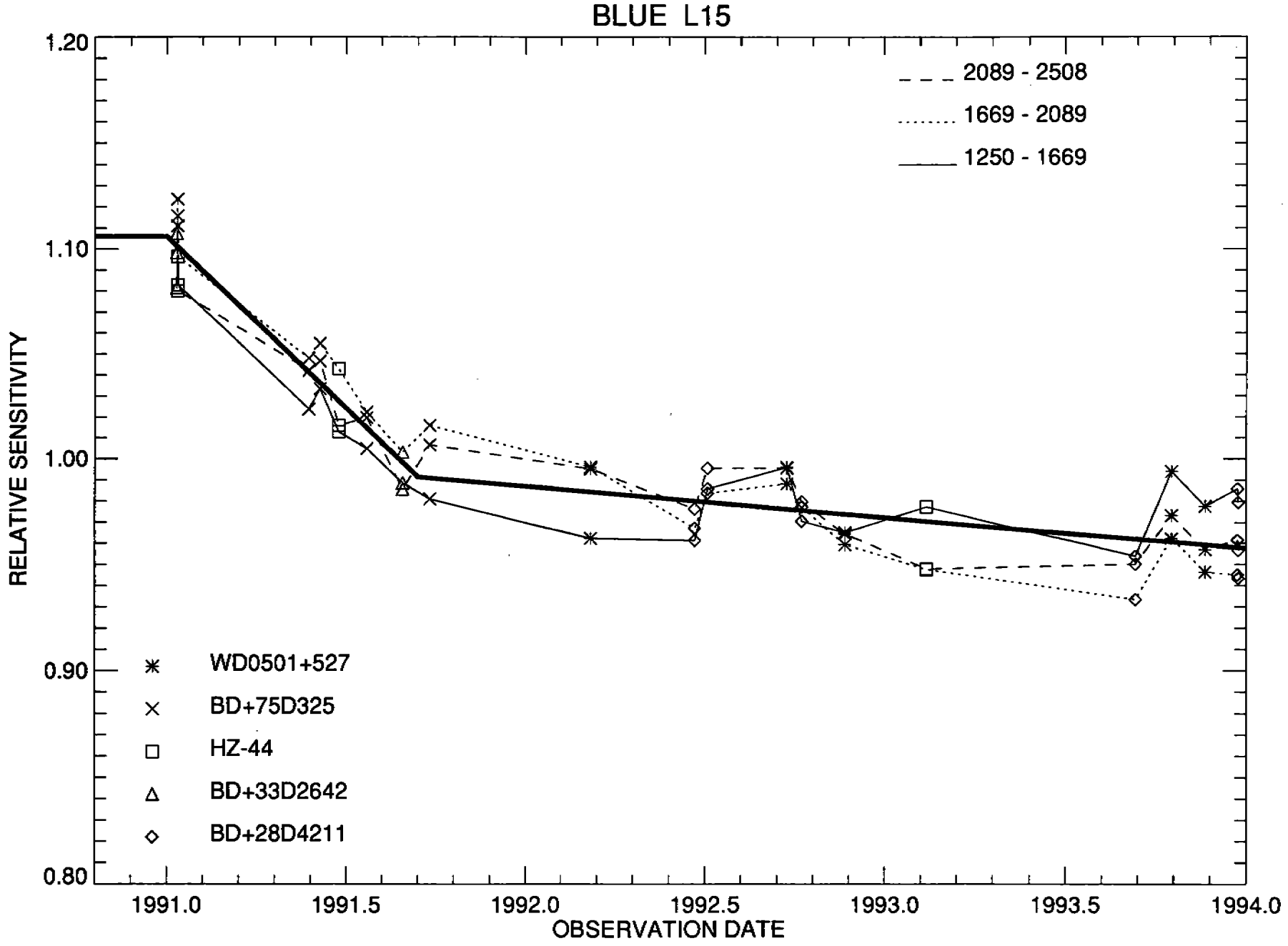
BLUE L15
1.20
1.10
1.00
0.90
0.80
RELATIVE SENSITIVITY
1991.0
1991.5
1992.0
1992.5
1993.0
1993.5
1994.0
OBSERVATION DATE
2089 - 2508
1669 - 2089
1250 - 1669
WD0501+527
BD+75D325
HZ-44
BD+33D2642
BD+28D4211

Fig. 3 (

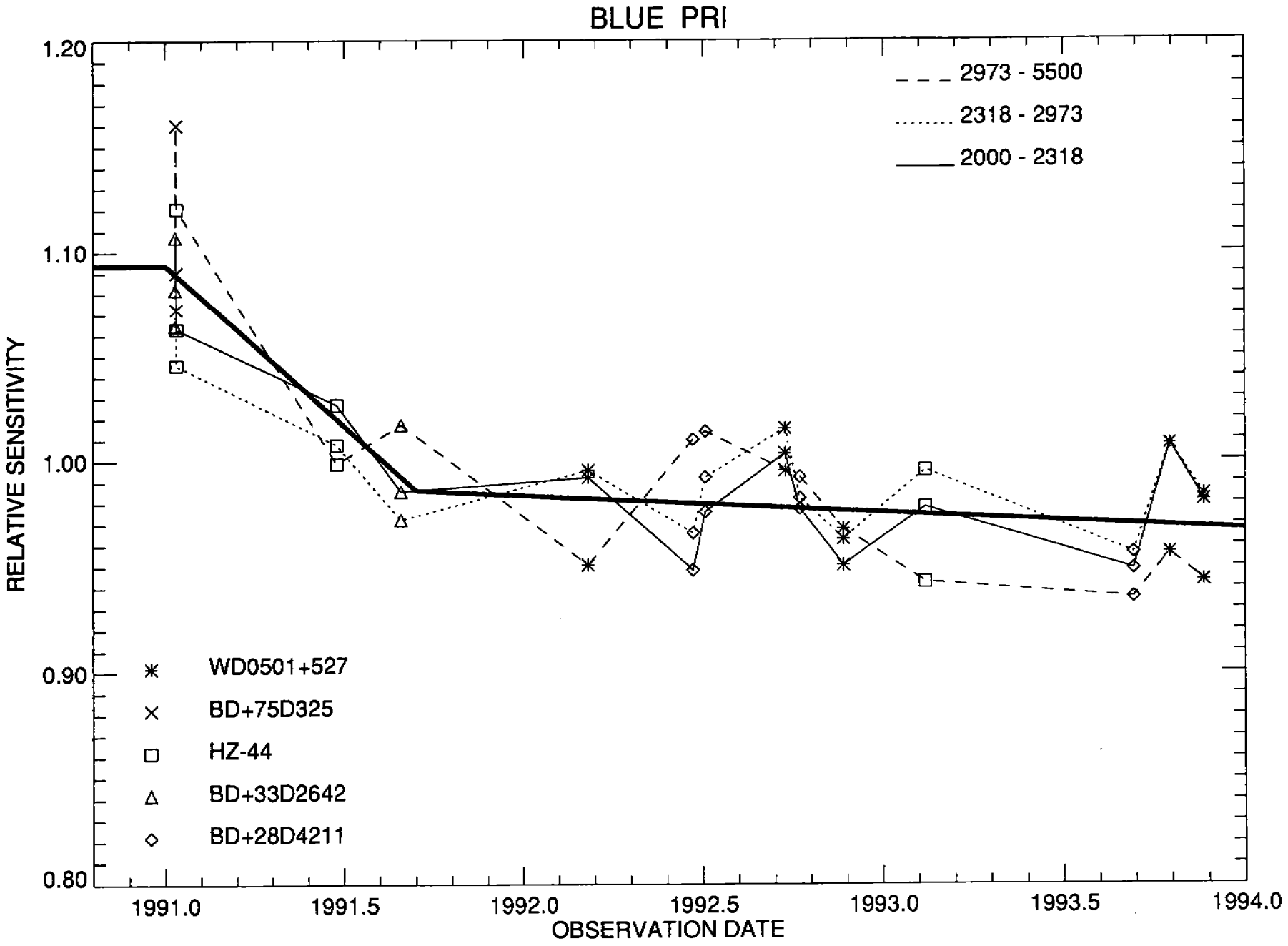

Fig. 3 (cont.)

PLTSENS_TIME 11-May-1994 06:21

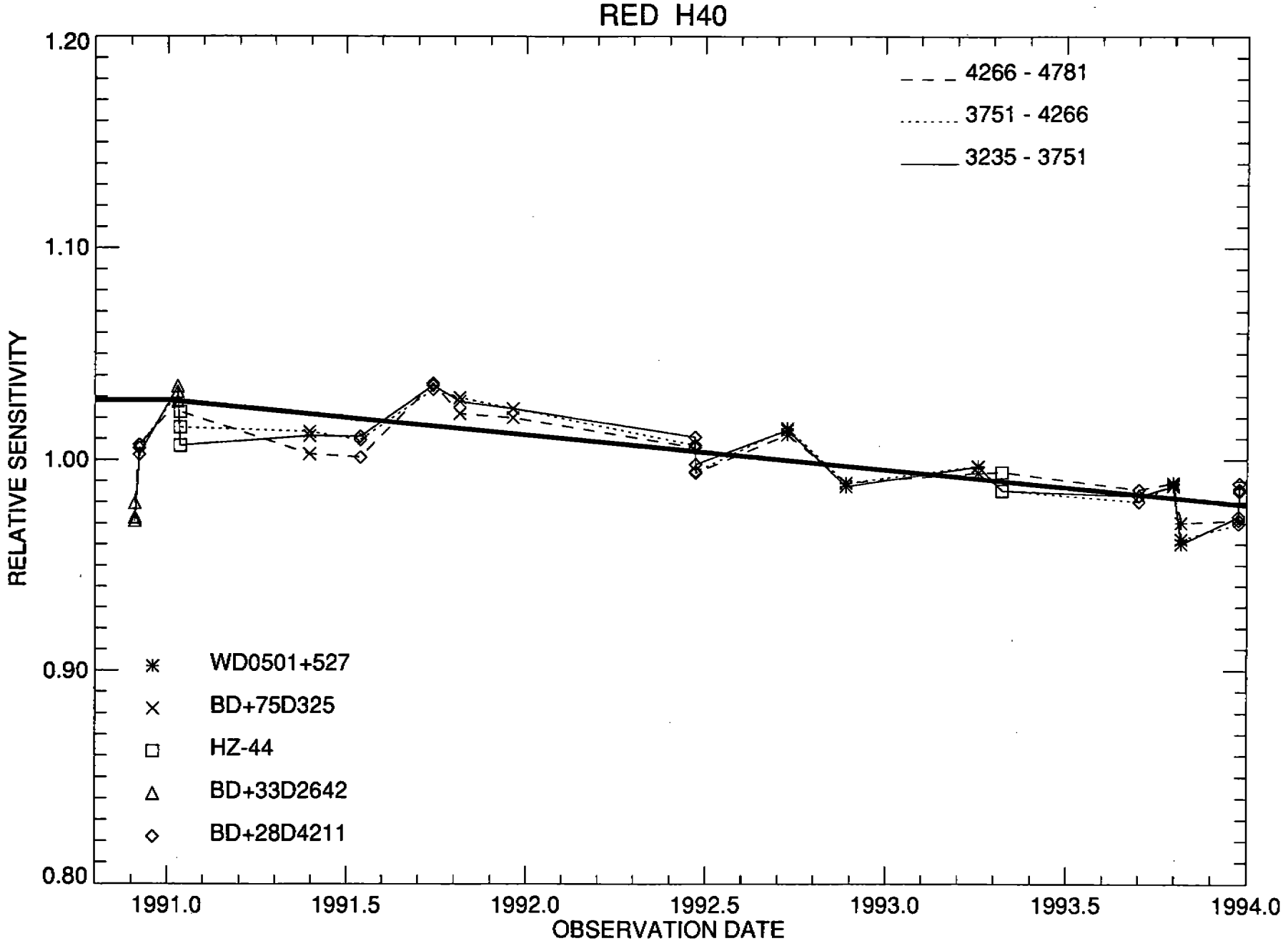
RED H40
1.20
1.10
1.00
0.90
0.80
RELATIVE SENSITIVITY
1991.0
1991.5
1992.0
1992.5
1993.0
1993.5
1994.0
OBSERVATION DATE
4266 - 4781
3751 - 4266
3235 - 3751
WD0501+527
BD+75D325
HZ-44
BD+33D2642
BD+28D4211

Fig. 3 (cont.)

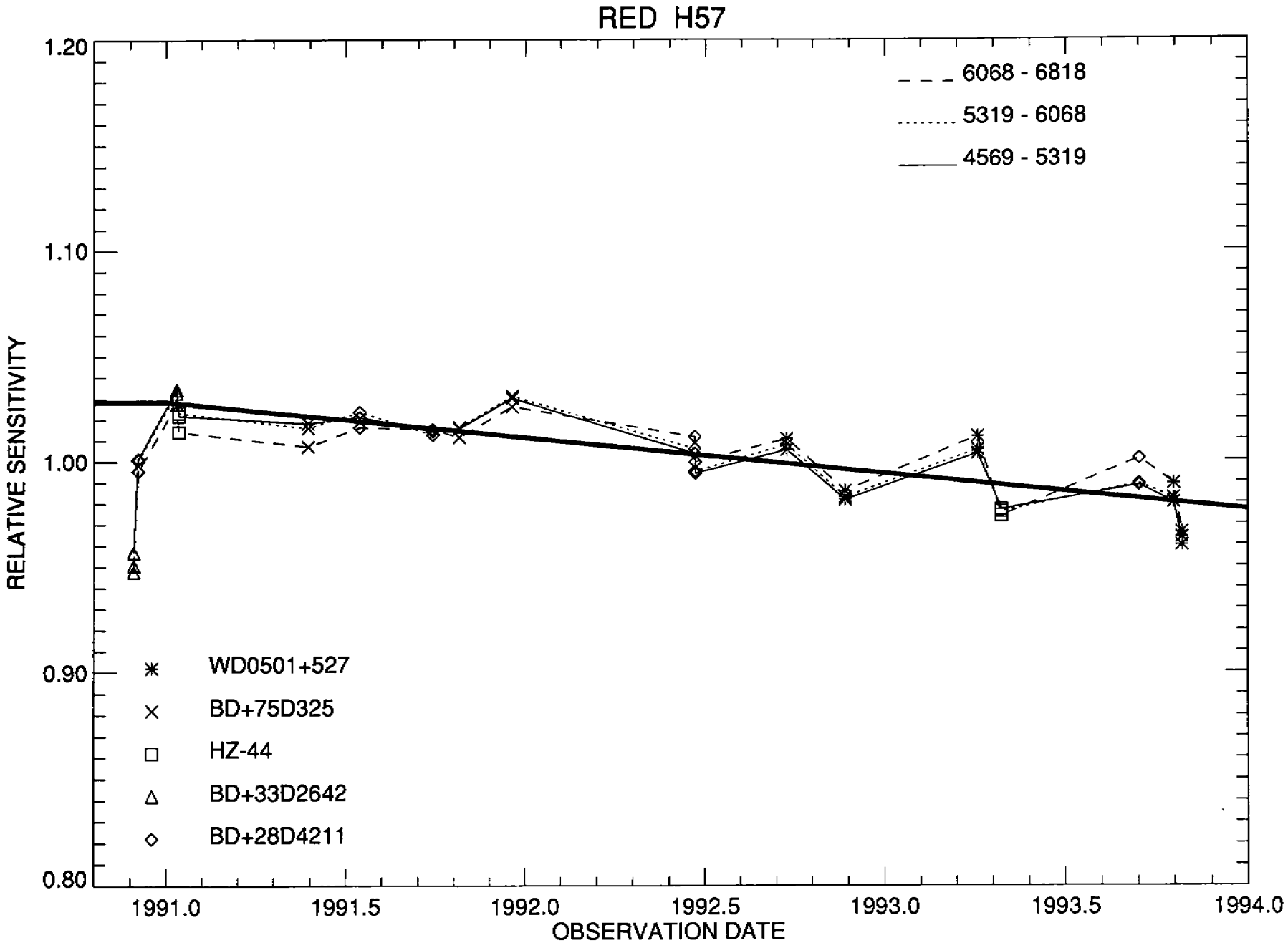

PLTSENS_TIME 11-May-1994 06:20

Fig. 3 (cont.)

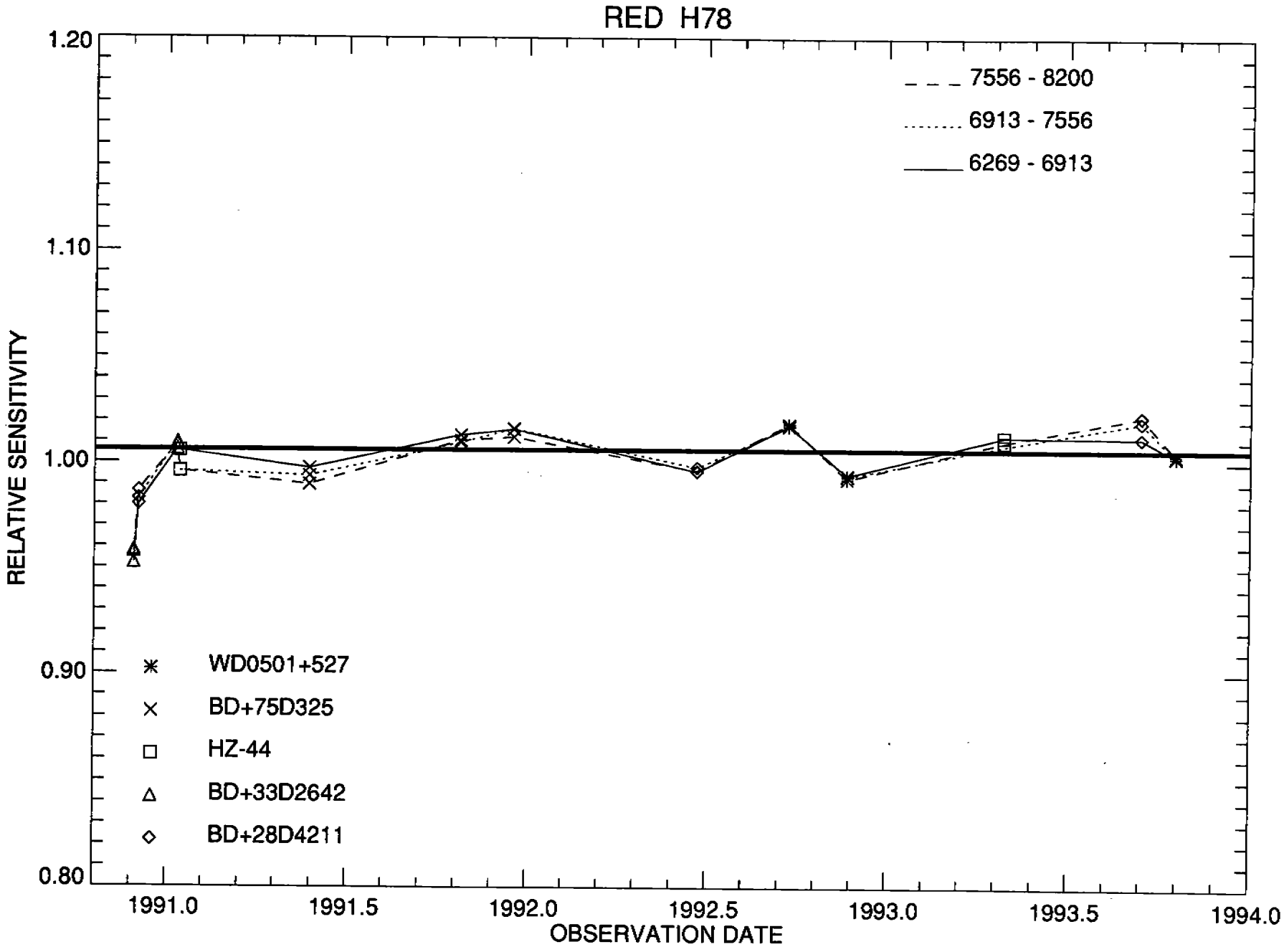
RED H78
1.20
1.10
1.00
0.90
0.80
RELATIVE SENSITIVITY
7556 - 8200
6913 - 7556
6269 - 6913
WD0501+527
BD+75D325
HZ-44
BD+33D2642
BD+28D4211
1991.0
1991.5
1992.0
1992.5
1993.0
1993.5
1994.0
OBSERVATION DATE

Fig. 3 (cont.)

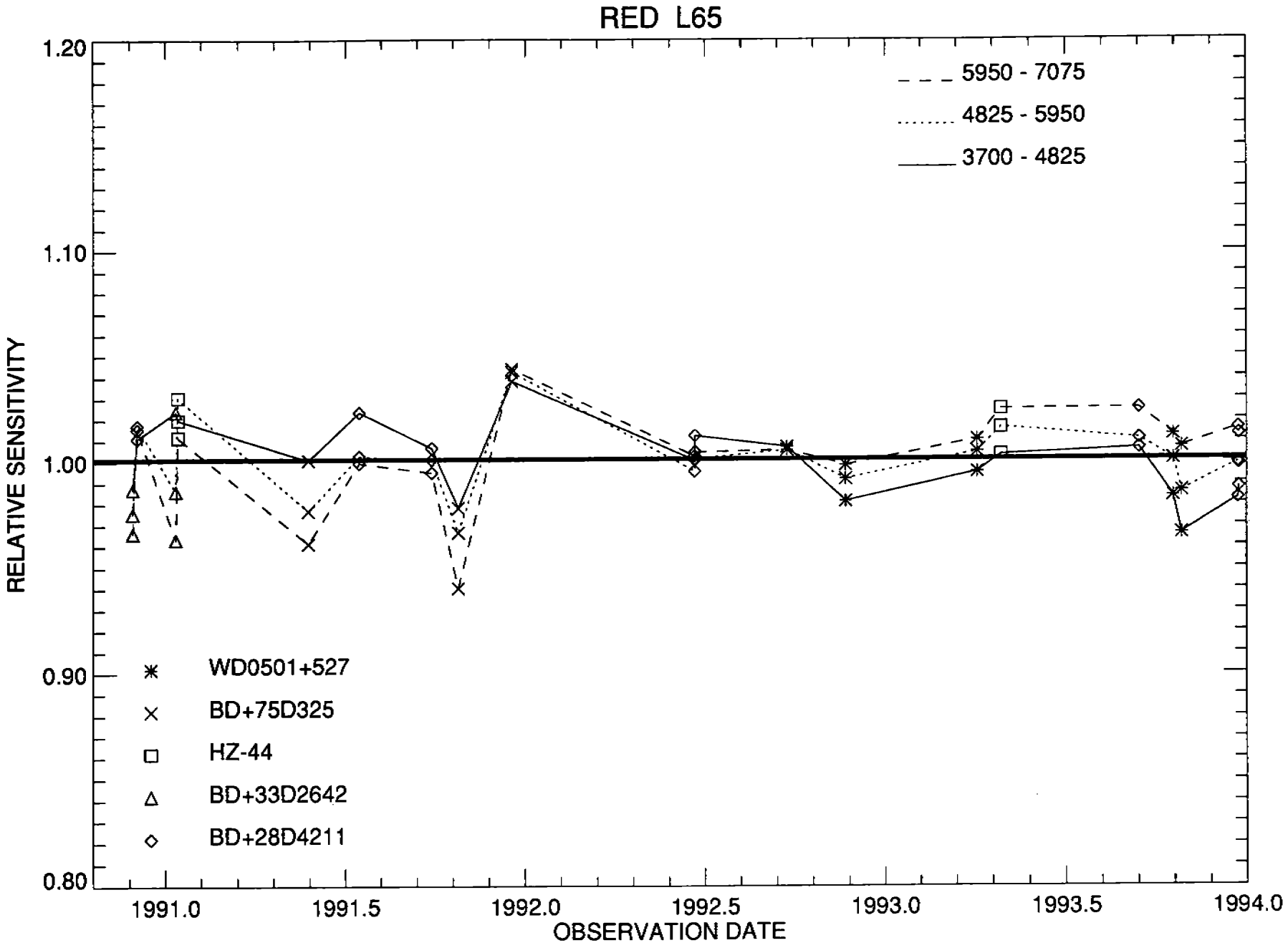

PLTSENS_TIME 11-May-1994 06:20

Fig. 3 (cont.)

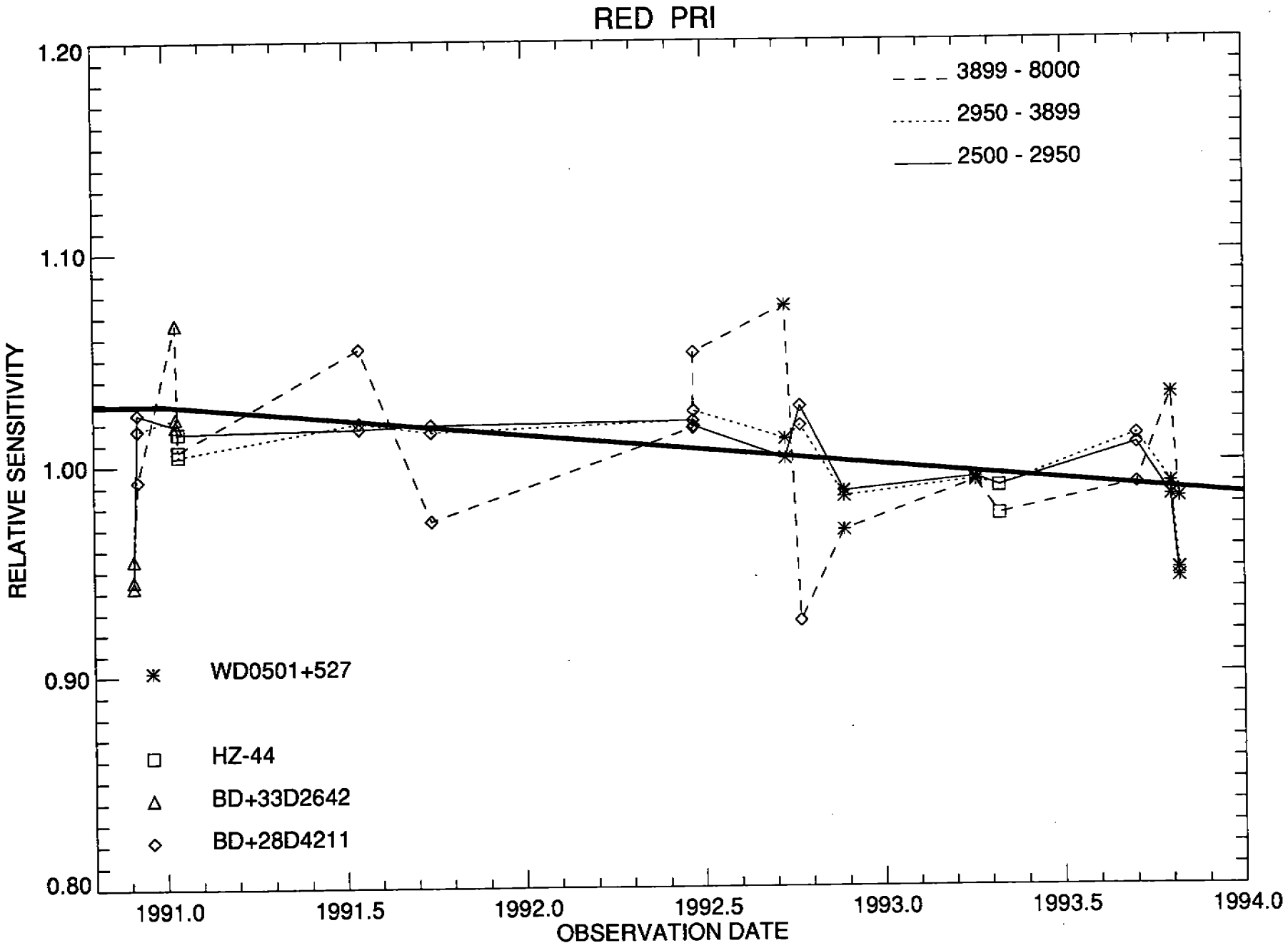
RED PRI
3899 - 8000
2950 - 3899
2500 - 2950
RELATIVE SENSITIVITY
1.20
1.10
1.00
0.90
0.80
WD0501+527
HZ-44
BD+33D2642
BD+28D4211
1991.0
1991.5
1992.0
1992.5
1993.0
1993.5
1994.0
OBSERVATION DATE

Fig. 3 (cont.)

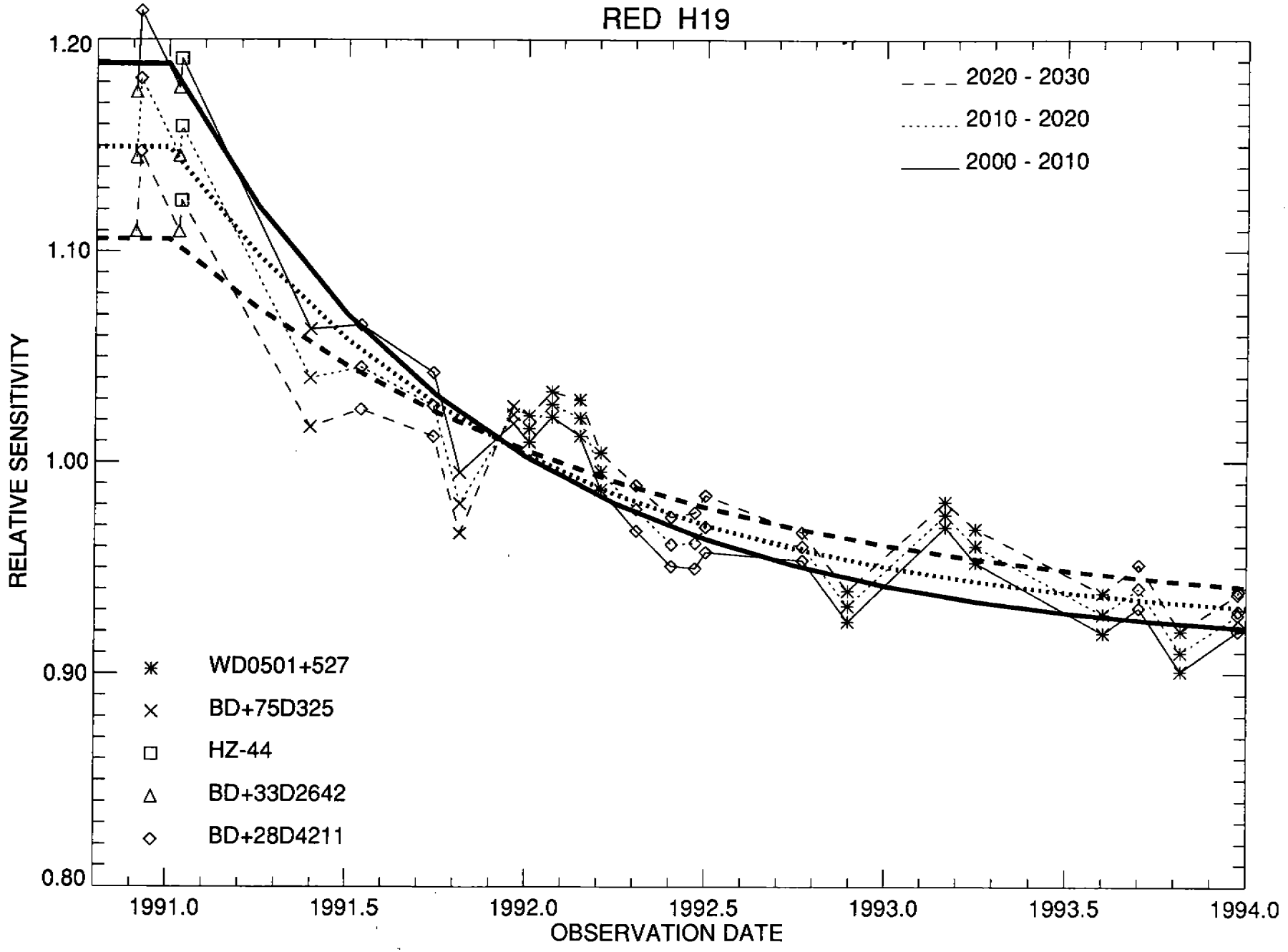

PLTSENS_TIME 10-Jun-1994 10:38

Fig. 4

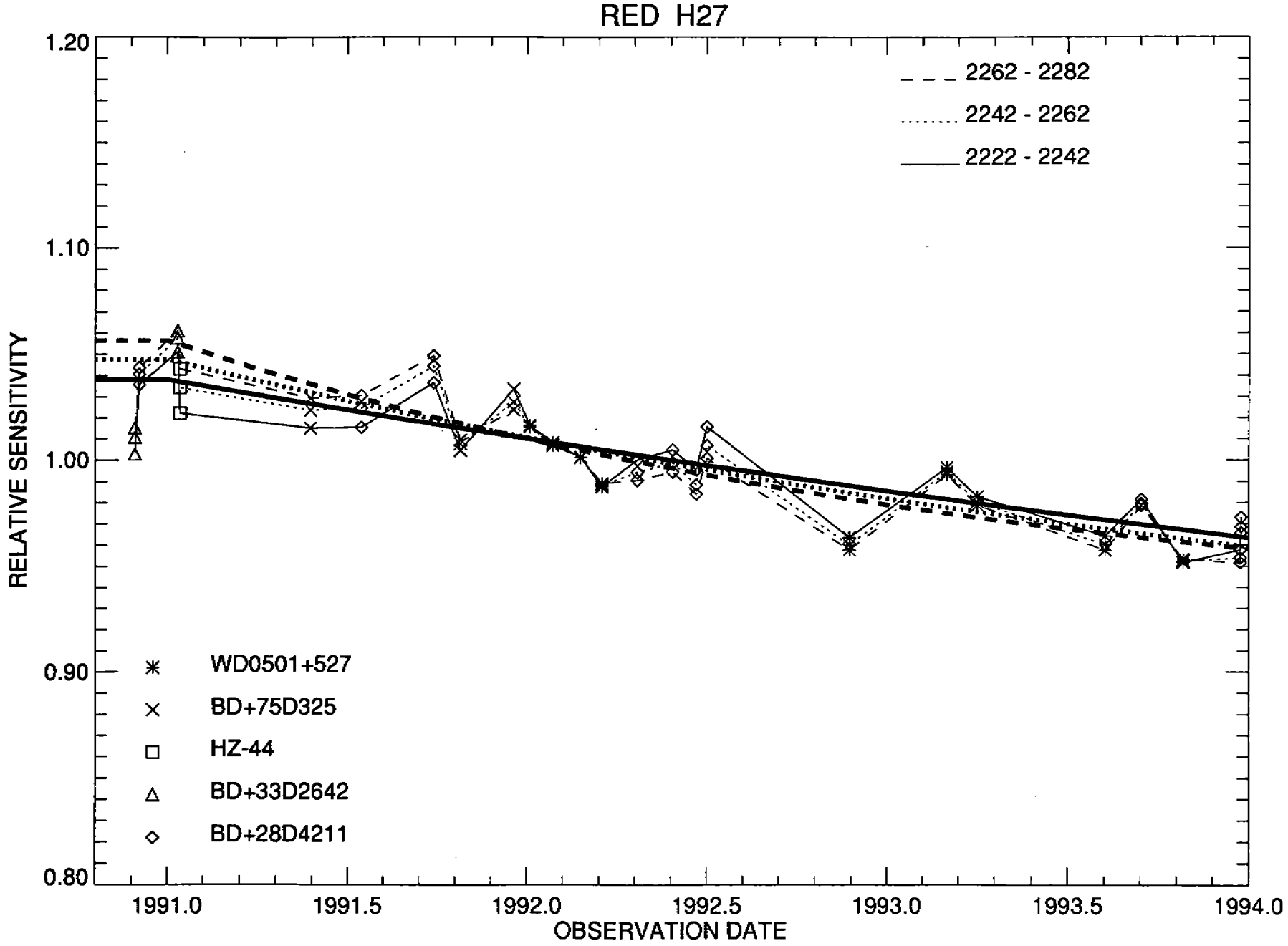
RED H27
1.20
1.10
1.00
0.90
0.80
RELATIVE SENSITIVITY
2262 - 2282
2242 - 2262
2222 - 2242
WD0501+527
BD+75D325
HZ-44
BD+33D2642
BD+28D4211
1991.0
1991.5
1992.0
1992.5
1993.0
1993.5
1994.0
OBSERVATION DATE

Fig. 4 (cont.)

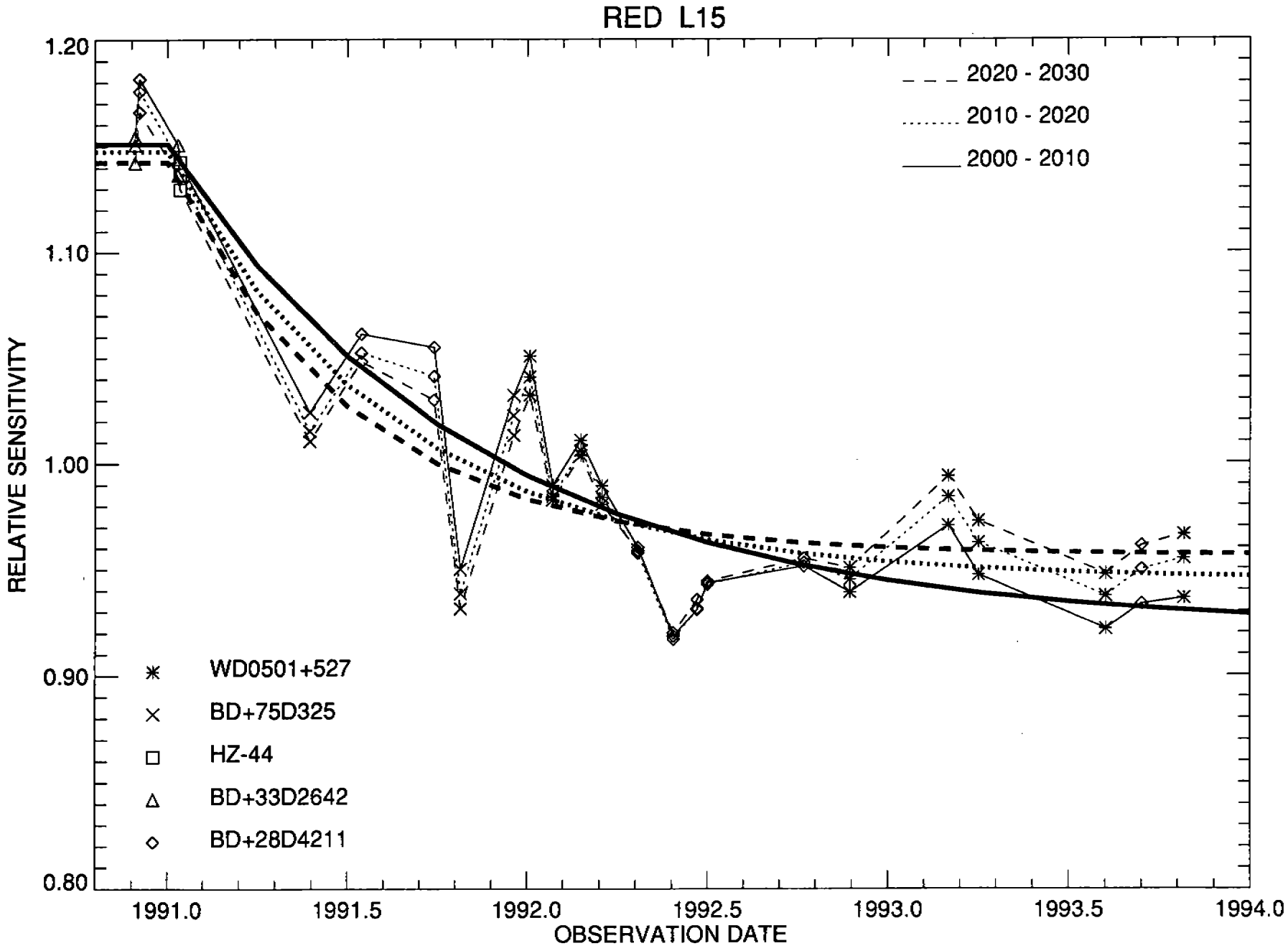

PLTSENS_TIME 11-May-1994 08:20

Fig. 4 (cont.)

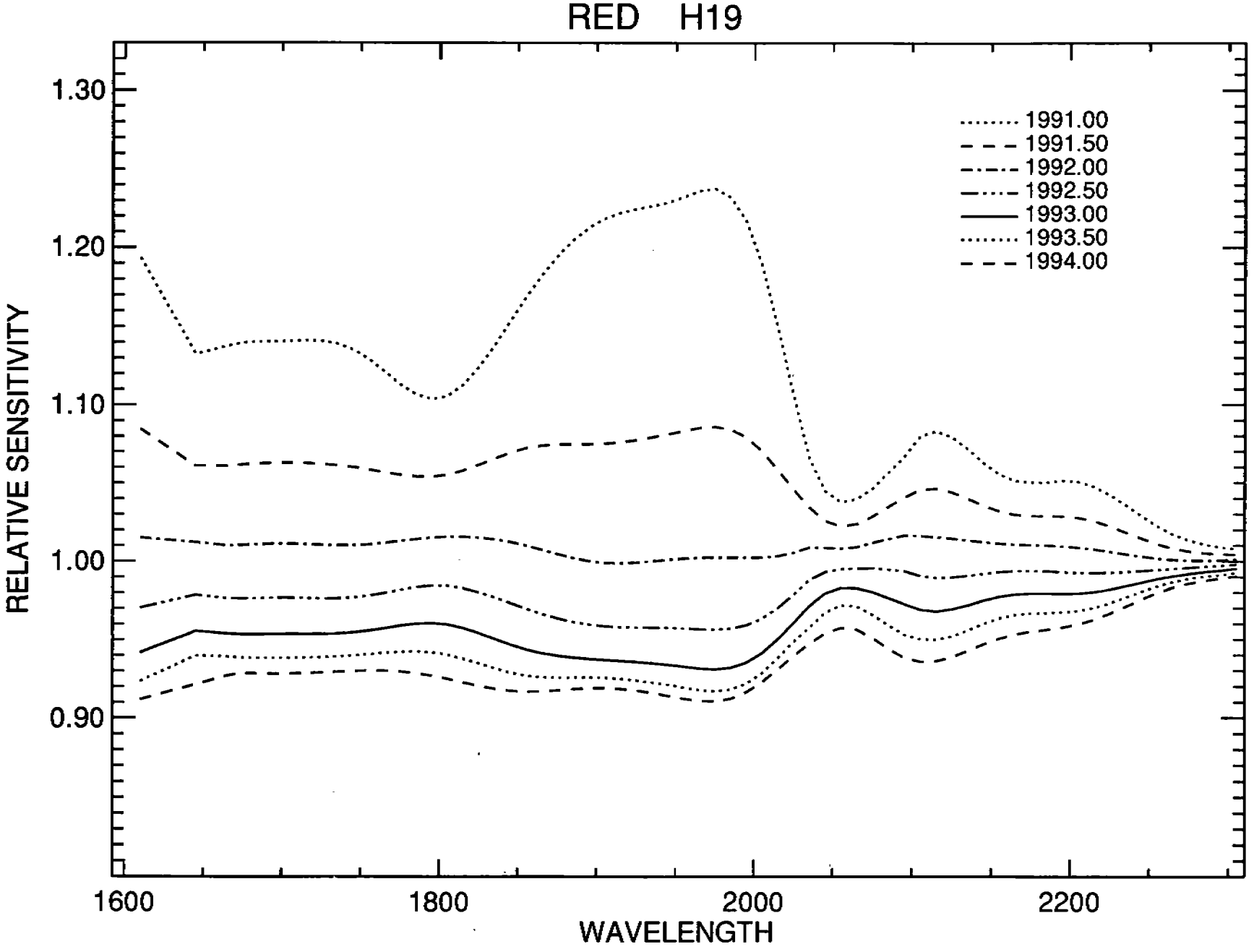
RED H19
RELATIVE SENSITIVITY
1.30
1.20
1.10
1.00
0.90
1600
1800
2000
2200
WAVELENGTH
1991.00
1991.50
1992.00
1992.50
1993.00
1993.50
1994.00

Fig 5a

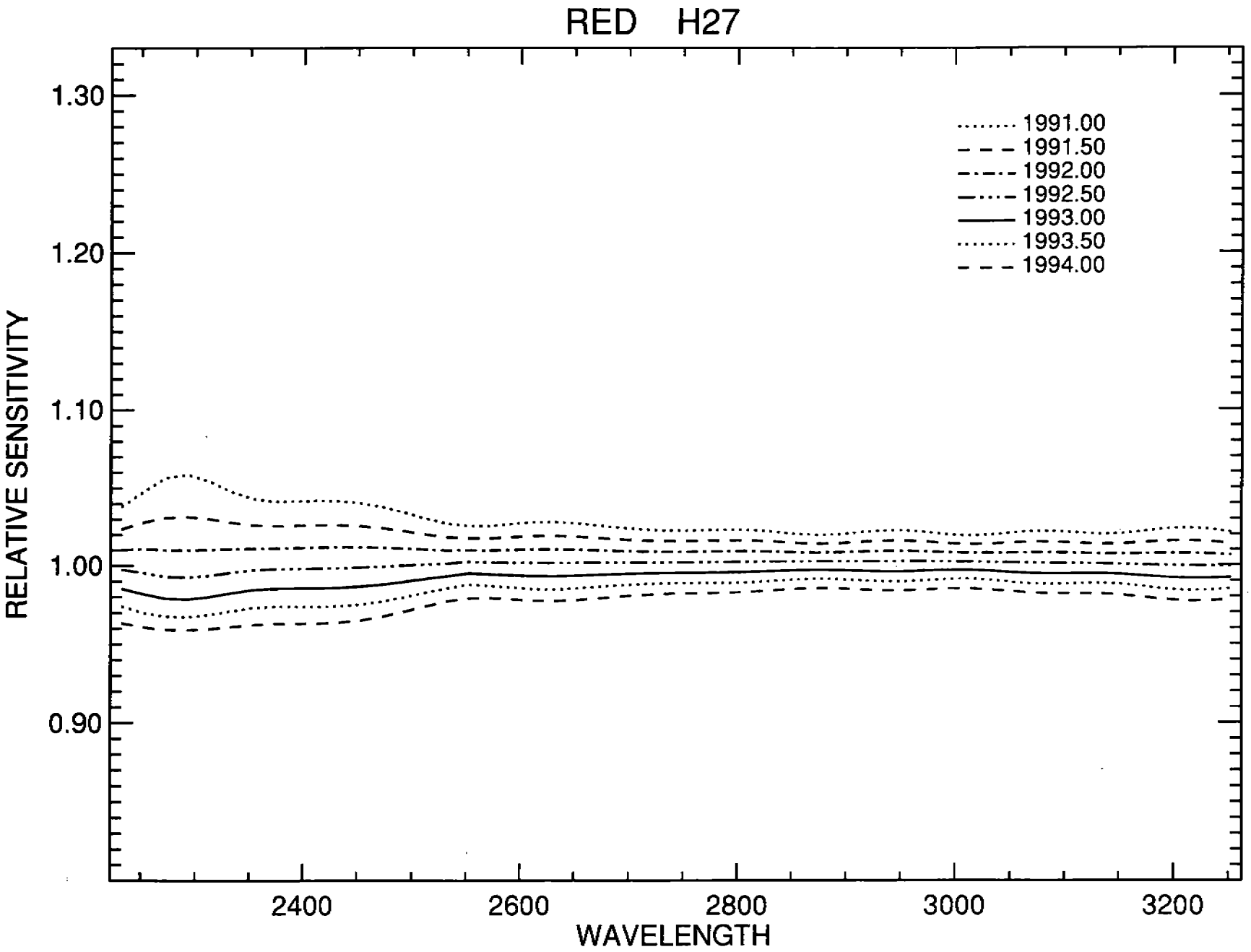
RED H27
1.30
1.20
1.10
1.00
0.90
RELATIVE SENSITIVITY
1991.00
1991.50
1992.00
1992.50
1993.00
1993.50
1994.00
2400
2600
2800
3000
3200
WAVELENGTH

Fig 5b

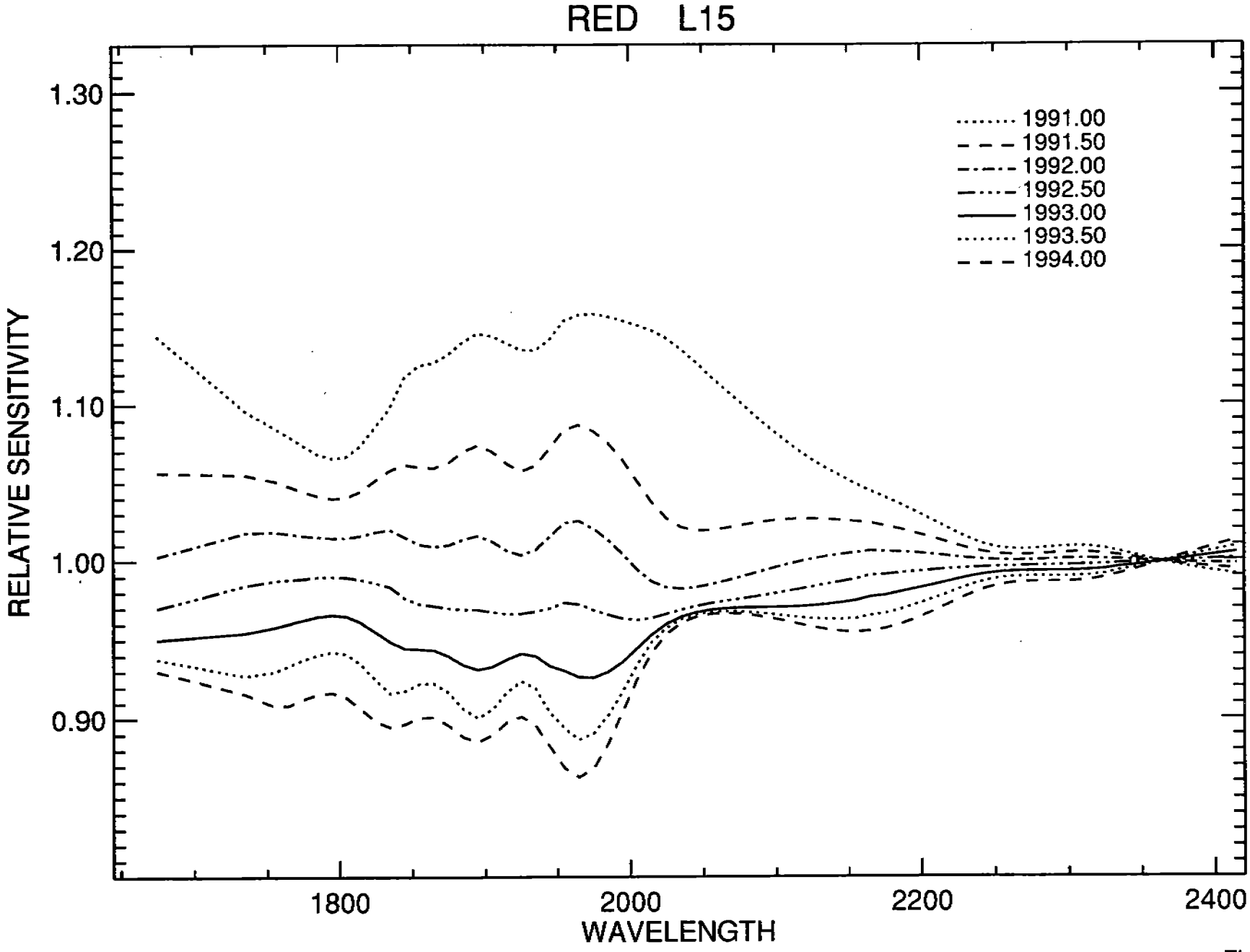
RED L15
1.30
1.20
1.10
1.00
0.90
RELATIVE SENSITIVITY
1800
2000
2200
2400
WAVELENGTH
1991.00
1991.50
1992.00
1992.50
1993.00
1993.50
1994.00

Fig 5c

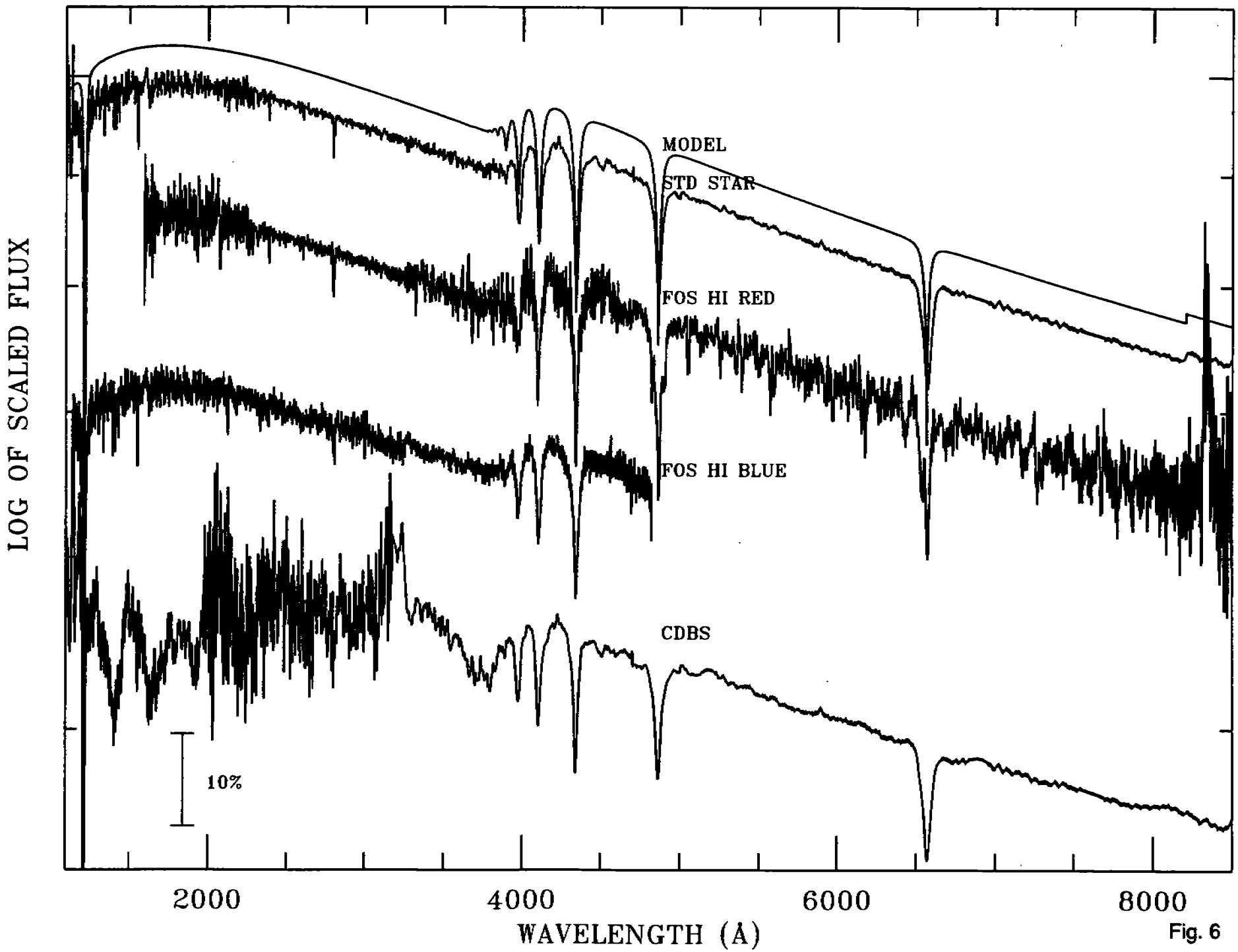
G191B2B
MODEL
STD STAR
FOS HI RED
FOS HI BLUE
CDBS
10%
LOG OF SCALED FLUX
2000
4000
6000
8000
WAVELENGTH (Å)

Fig. 6

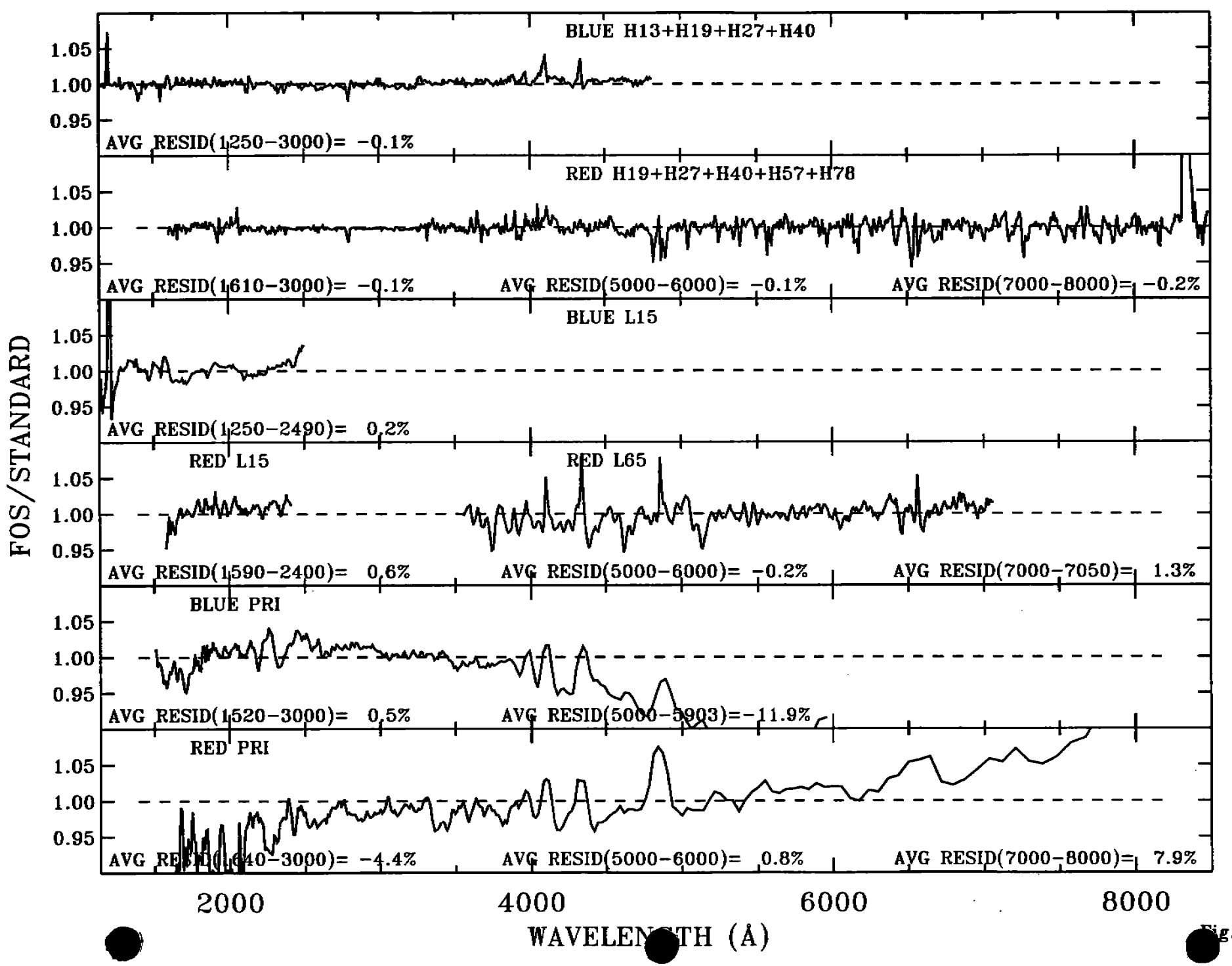
G191B2B
BLUE H13+H19+H27+H40
AVG RESID(1250-3000)= -0.1%
RED H19+H27+H40+H57+H78
AVG RESID(1610-3000)= -0.1%
AVG RESID(5000-6000)= -0.1%
AVG RESID(7000-8000)= -0.2%
BLUE L15
AVG RESID(1250-2490)= 0.2%
RED L15
AVG RESID(1590-2400)= 0.6%
RED L65
AVG RESID(5000-6000)= -0.2%
AVG RESID(7000-7050)= 1.3%
BLUE PRI
AVG RESID(1520-3000)= 0.5%
AVG RESID(5000-5903)=-11.9%
RED PRI
AVG RESID(1640-3000)= -4.4%
AVG RESID(5000-6000)= 0.8%
AVG RESID(7000-8000)= 7.9%
1.05
1.00
0.95
FOS/STANDARD
2000
4000
6000
8000
WAVELENGTH (Å)

Fig. 7a

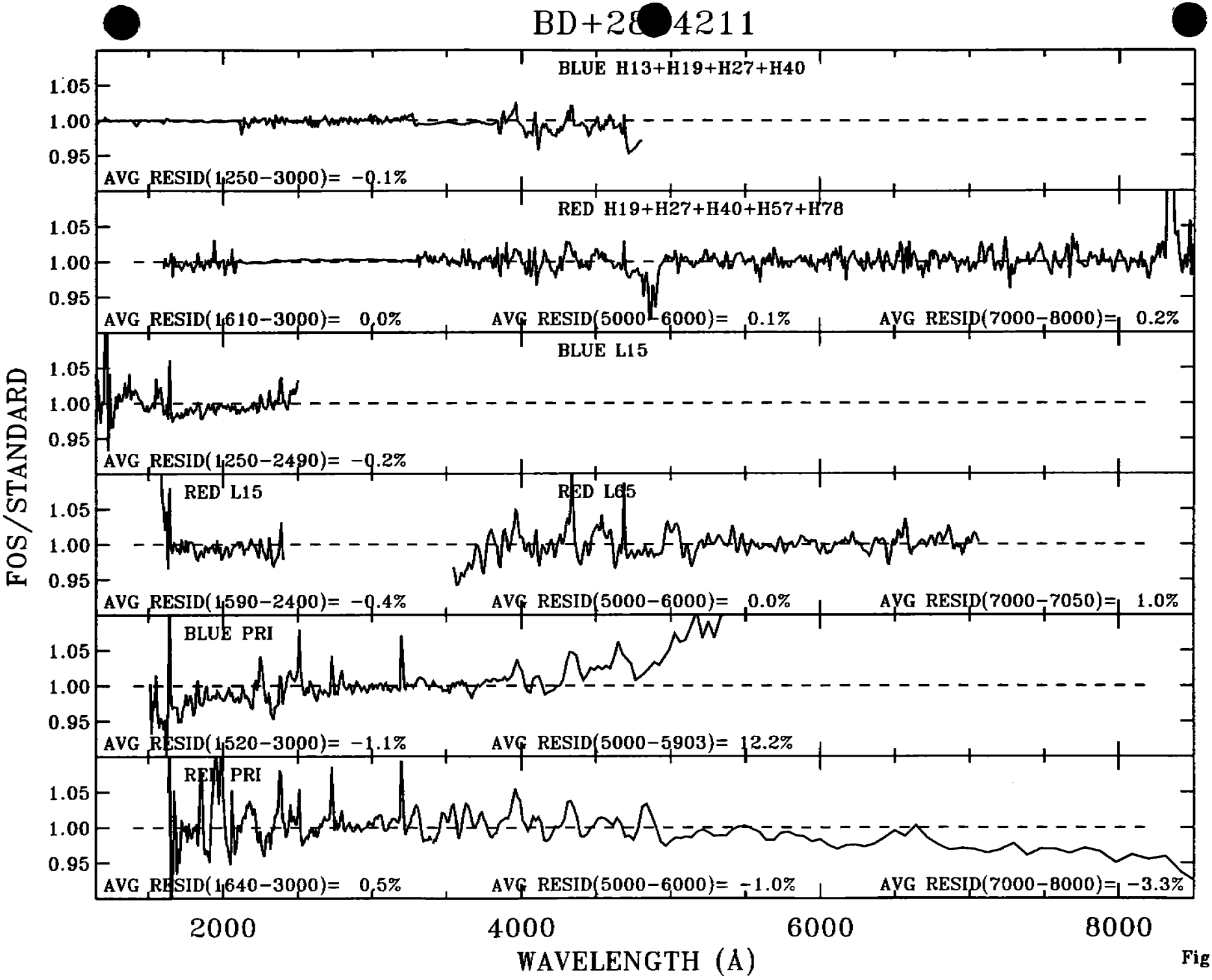
BD+28 4211
BLUE H13+H19+H27+H40
AVG RESID(1250-3000)= -0.1%
RED H19+H27+H40+H57+H78
AVG RESID(1610-3000)= 0.0%
AVG RESID(5000-6000)= 0.1%
AVG RESID(7000-8000)= 0.2%
BLUE L15
AVG RESID(1250-2490)= -0.2%
RED L15
RED L65
AVG RESID(1590-2400)= -0.4%
AVG RESID(5000-6000)= 0.0%
AVG RESID(7000-7050)= 1.0%
BLUE PRI
AVG RESID(1520-3000)= -1.1%
AVG RESID(5000-5903)= 12.2%
RED PRI
AVG RESID(1640-3000)= 0.5%
AVG RESID(5000-6000)= -1.0%
AVG RESID(7000-8000)= -3.3%
FOS/STANDARD
1.05
1.00
0.95
2000
4000
6000
8000
WAVELENGTH (Å)

Fig. 7b

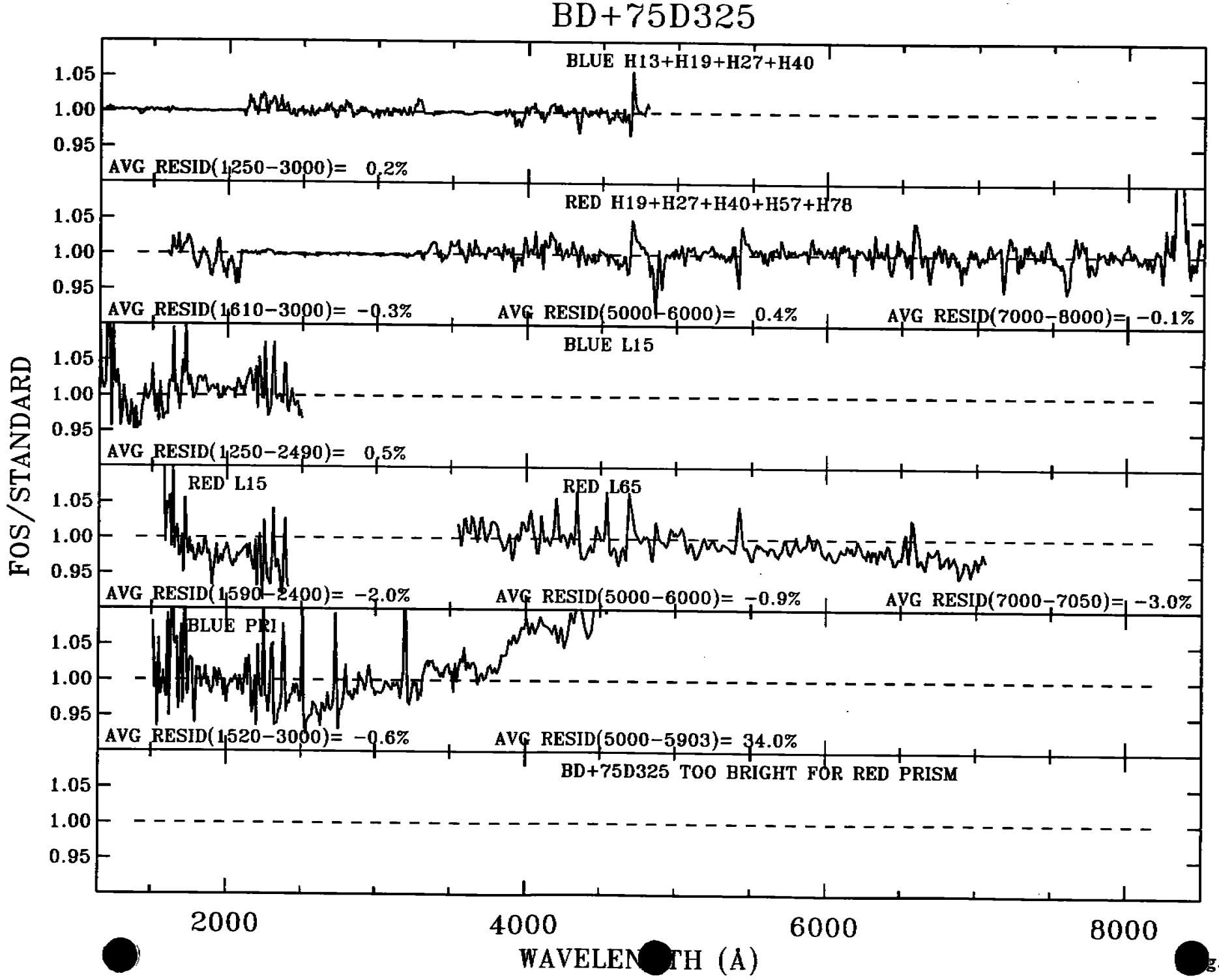
BD+75D325
BLUE H13+H19+H27+H40
AVG RESID(1250-3000)= 0.2%
RED H19+H27+H40+H57+H78
AVG RESID(1610-3000)= -0.3%
AVG RESID(5000-6000)= 0.4%
AVG RESID(7000-8000)= -0.1%
BLUE L15
AVG RESID(1250-2490)= 0.5%
RED L15
RED L65
AVG RESID(1590-2400)= -2.0%
AVG RESID(5000-6000)= -0.9%
AVG RESID(7000-7050)= -3.0%
BLUE PRI
AVG RESID(1520-3000)= -0.6%
AVG RESID(5000-5903)= 34.0%
BD+75D325 TOO BRIGHT FOR RED PRISM
FOS/STANDARD
1.05
1.00
0.95
2000
4000
6000
8000
WAVELENGTH (A)

Fig. 7c

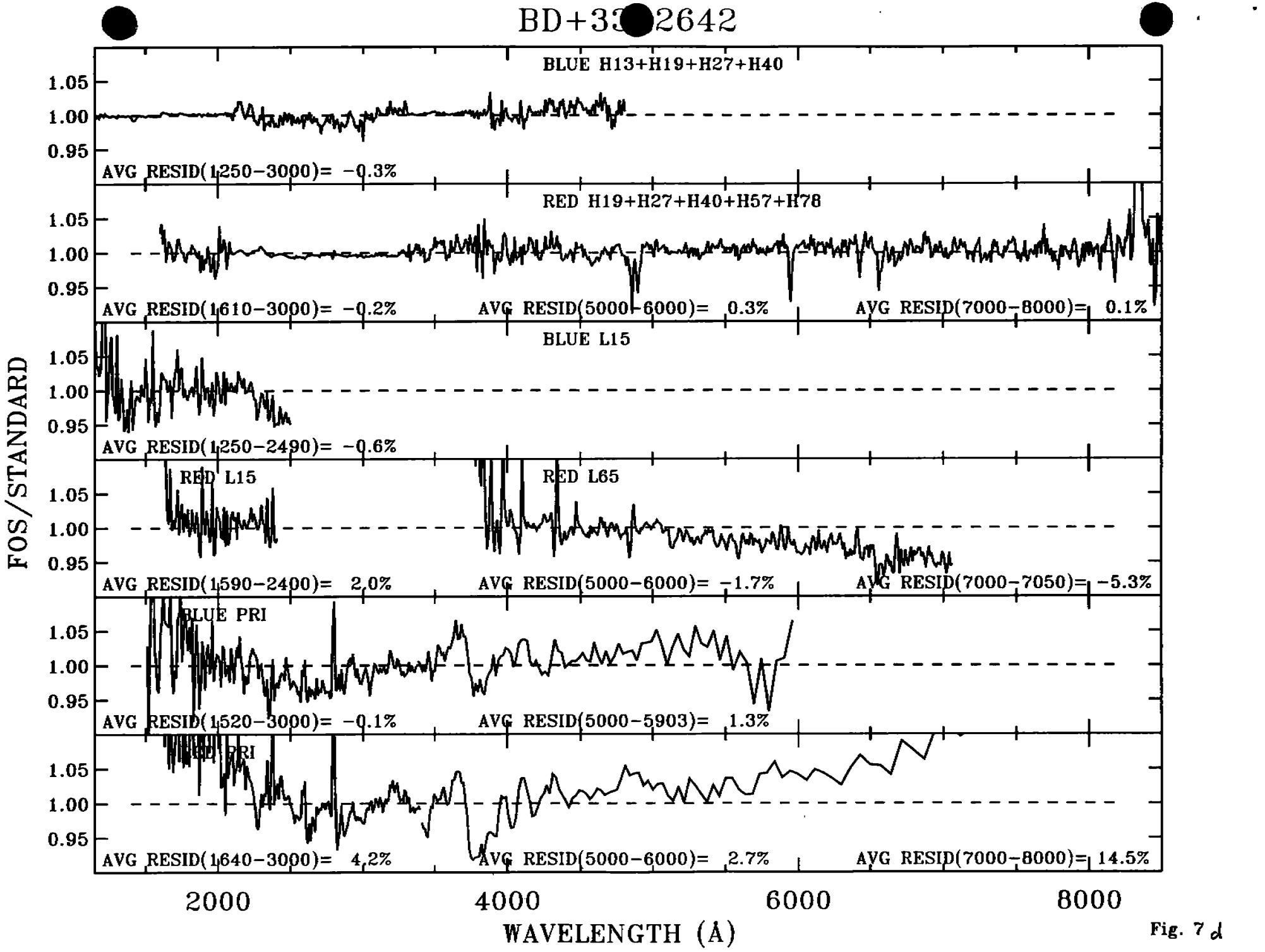
BD+33 2642
BLUE H13+H19+H27+H40
AVG RESID(1250-3000)= -0.3%
RED H19+H27+H40+H57+H78
AVG RESID(1610-3000)= -0.2%
AVG RESID(5000-6000)= 0.3%
AVG RESID(7000-8000)= 0.1%
BLUE L15
AVG RESID(1250-2490)= -0.6%
RED L15
RED L65
AVG RESID(1590-2400)= 2.0%
AVG RESID(5000-6000)= -1.7%
AVG RESID(7000-7050)= -5.3%
BLUE PRI
AVG RESID(1520-3000)= -0.1%
AVG RESID(5000-5903)= 1.3%
RED PRI
AVG RESID(1640-3000)= 4.2%
AVG RESID(5000-6000)= 2.7%
AVG RESID(7000-8000)= 14.5%
1.05
1.00
0.95
FOS/STANDARD
2000
4000
6000
8000
WAVELENGTH (Å)

Fig. 7 d

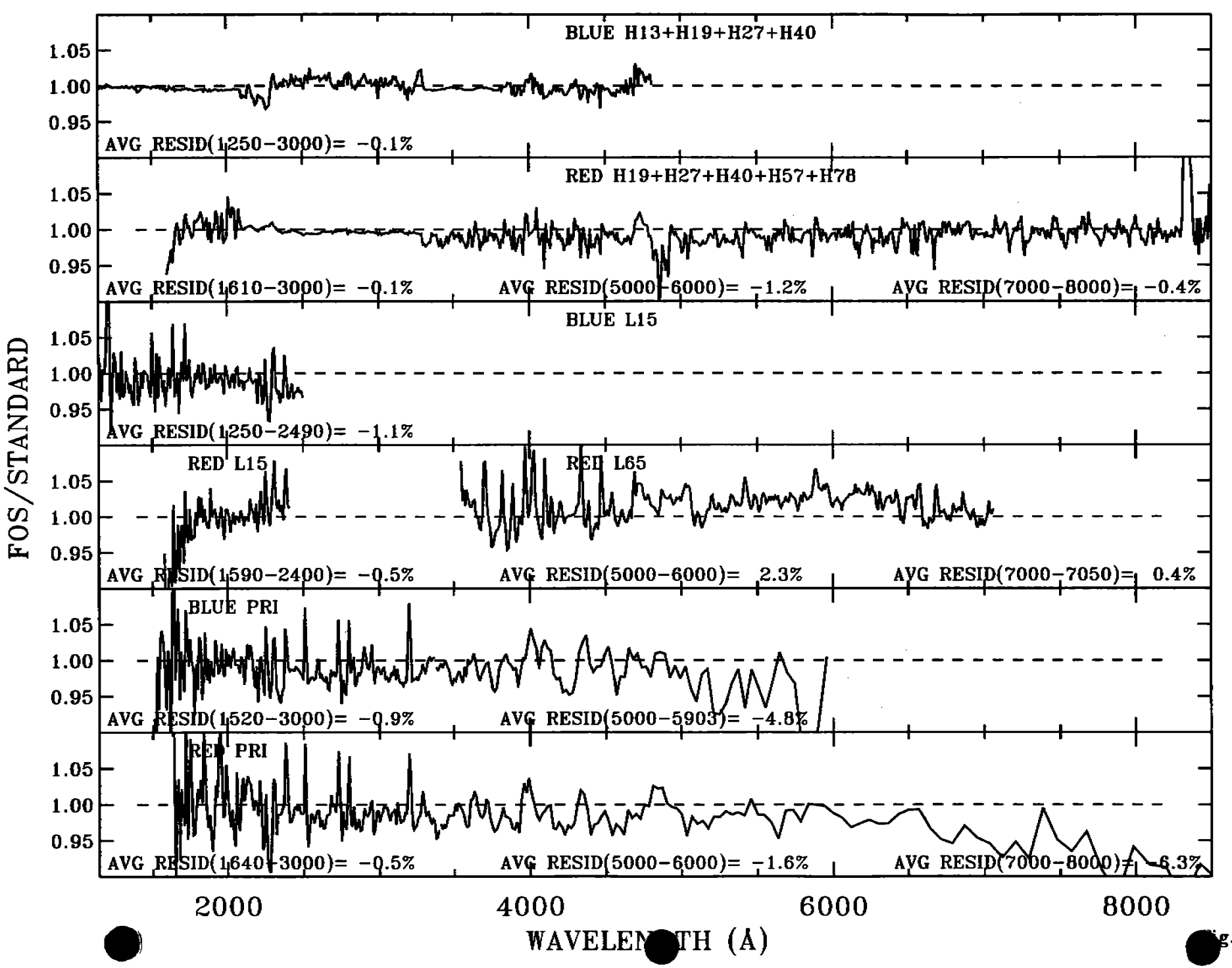
HZ-44
BLUE H13+H19+H27+H40
AVG RESID(1250-3000)= -0.1%
RED H19+H27+H40+H57+H78
AVG RESID(1610-3000)= -0.1%
AVG RESID(5000-6000)= -1.2%
AVG RESID(7000-8000)= -0.4%
BLUE L15
AVG RESID(1250-2490)= -1.1%
RED L15
RED L65
AVG RESID(1590-2400)= -0.5%
AVG RESID(5000-6000)= 2.3%
AVG RESID(7000-7050)= 0.4%
BLUE PRI
AVG RESID(1520-3000)= -0.9%
AVG RESID(5000-5903)= -4.8%
RED PRI
AVG RESID(1640-3000)= -0.5%
AVG RESID(5000-6000)= -1.6%
AVG RESID(7000-8000)= -6.3%
1.05
1.00
0.95
FOS/STANDARD
2000
4000
6000
8000
WAVELENGTH (Å)

Fig. 7e

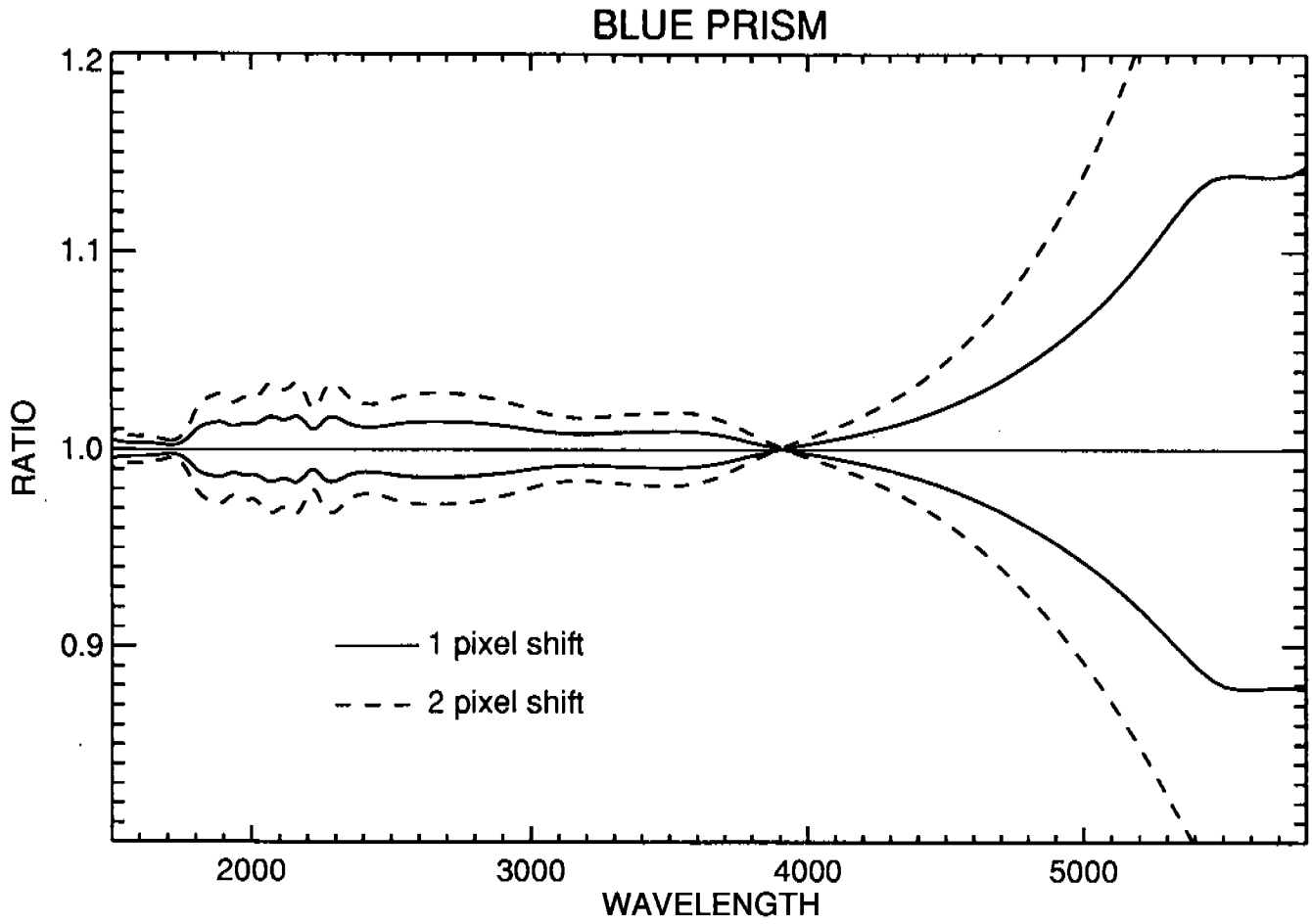
BLUE PRISM
1.2
1.1
1.0
0.9
RATIO
1 pixel shift
2 pixel shift
2000
3000
4000
5000
WAVELENGTH

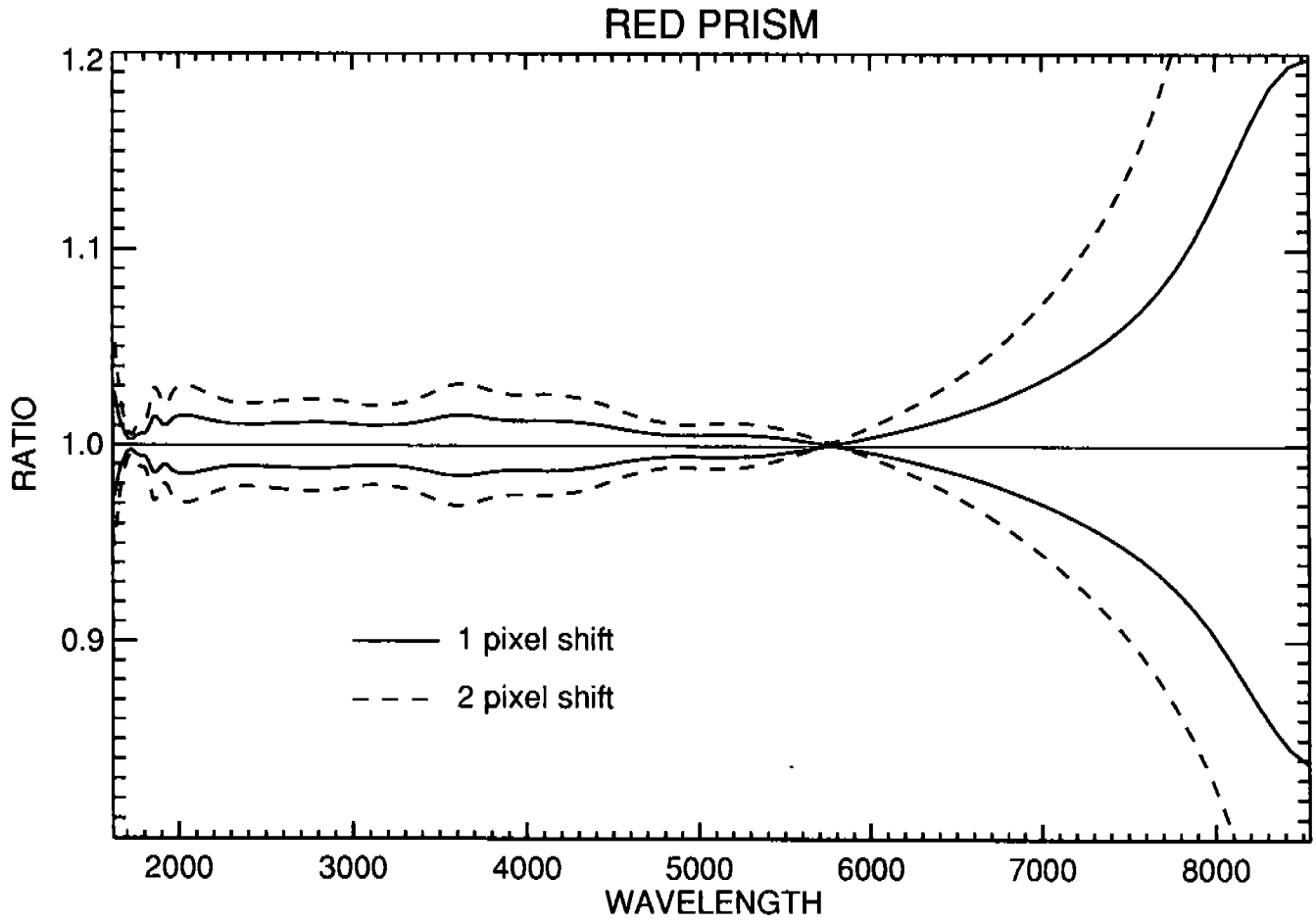
RED PRISM
1.2
1.1
1.0
0.9
RATIO
1 pixel shift
2 pixel shift
2000
3000
4000
5000
6000
7000
8000
WAVELENGTH

Fig. 8

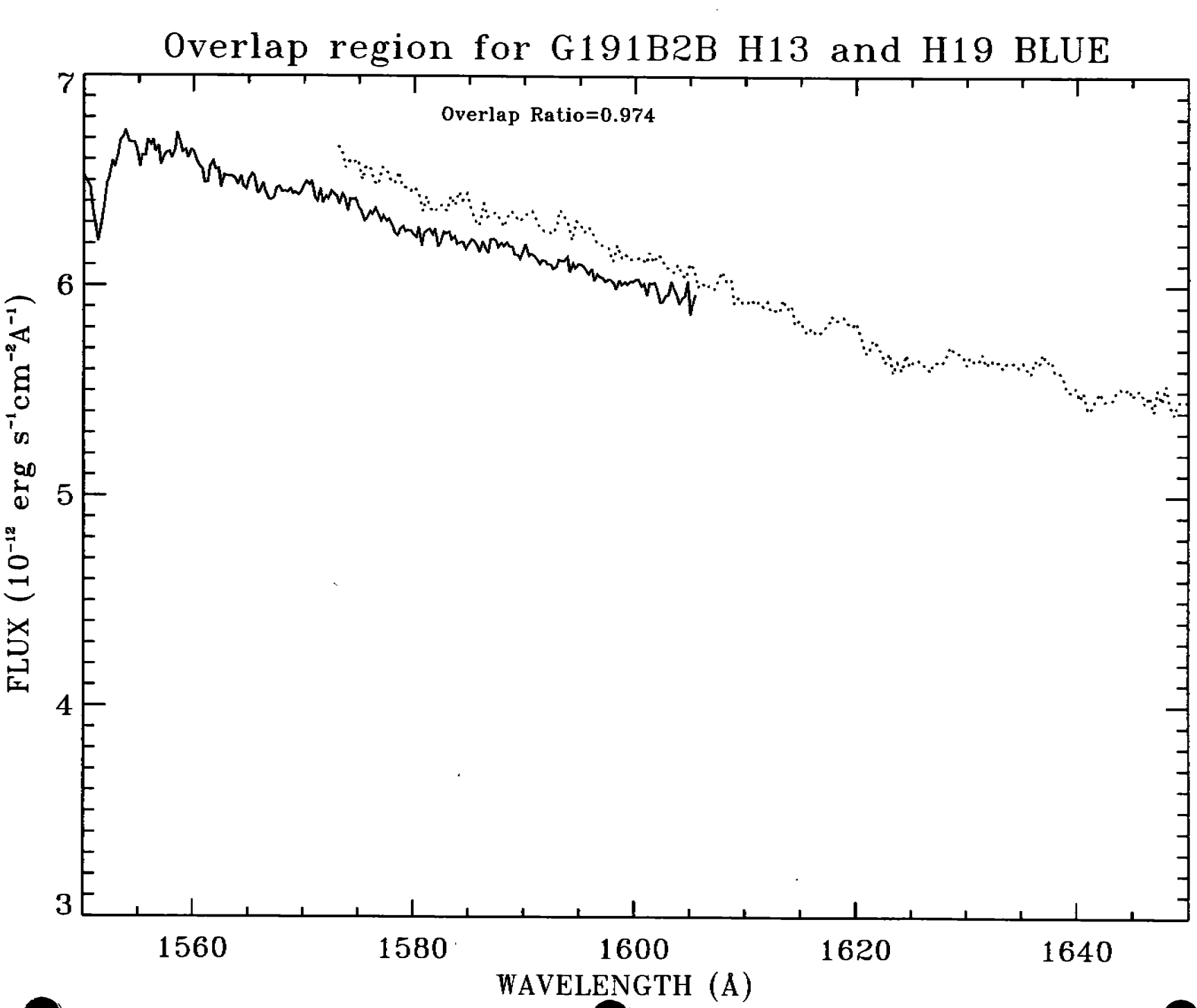
Overlap region for G191B2B H13 and H19 BLUE
Overlap Ratio=0.974
FLUX (10^{-12} erg $s^{-1}cm^{-2}A^{-1}$)
WAVELENGTH (A)
7
6
5
4
3
1560
1580
1600
1620
1640

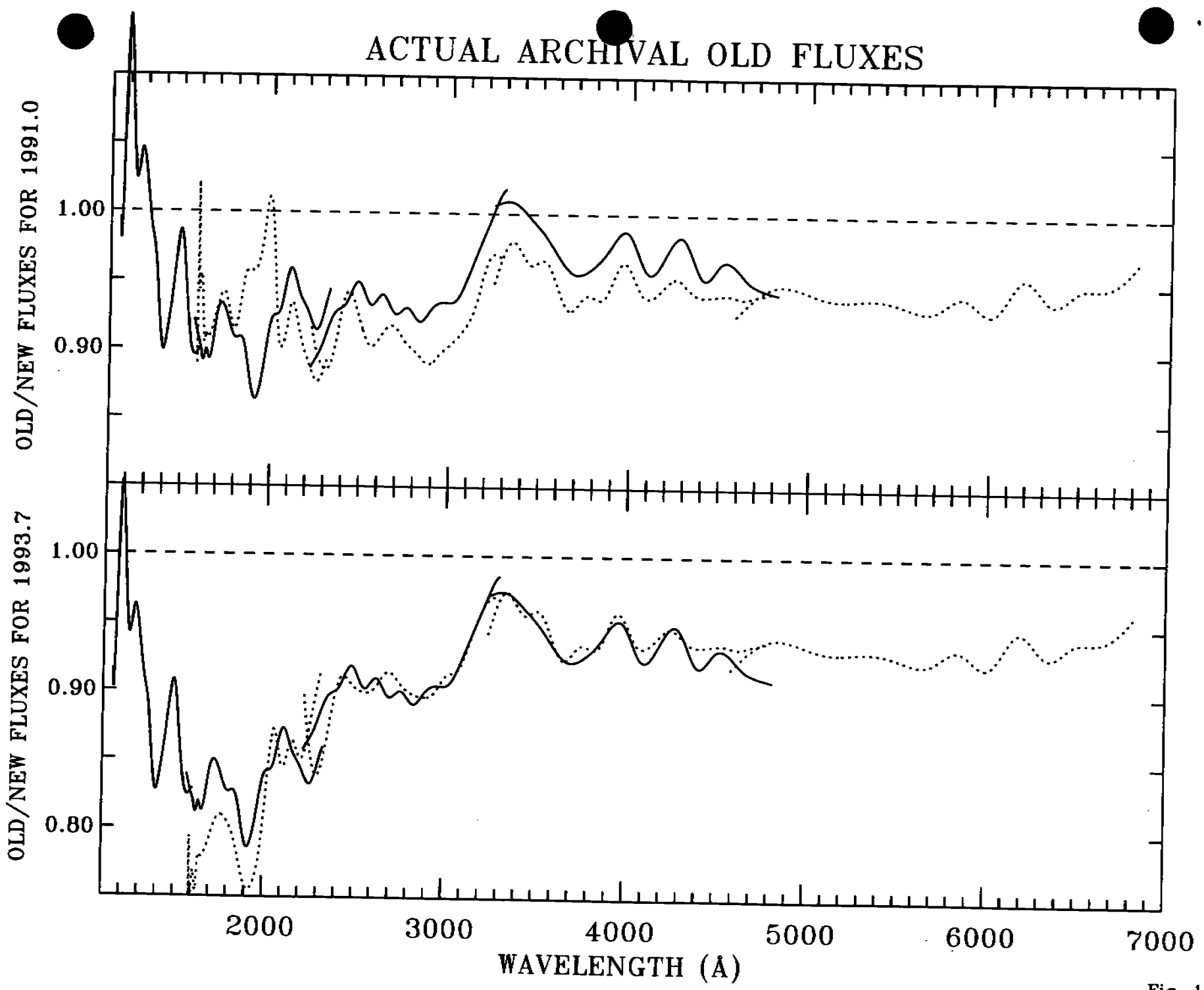
ACTUAL ARCHIVAL OLD FLUXES
OLD/NEW FLUXES FOR 1991.0
1.00
0.90
OLD/NEW FLUXES FOR 1993.7
1.00
0.90
0.80
2000
3000
4000
5000
6000
7000
WAVELENGTH (Å)

Fig. 10a

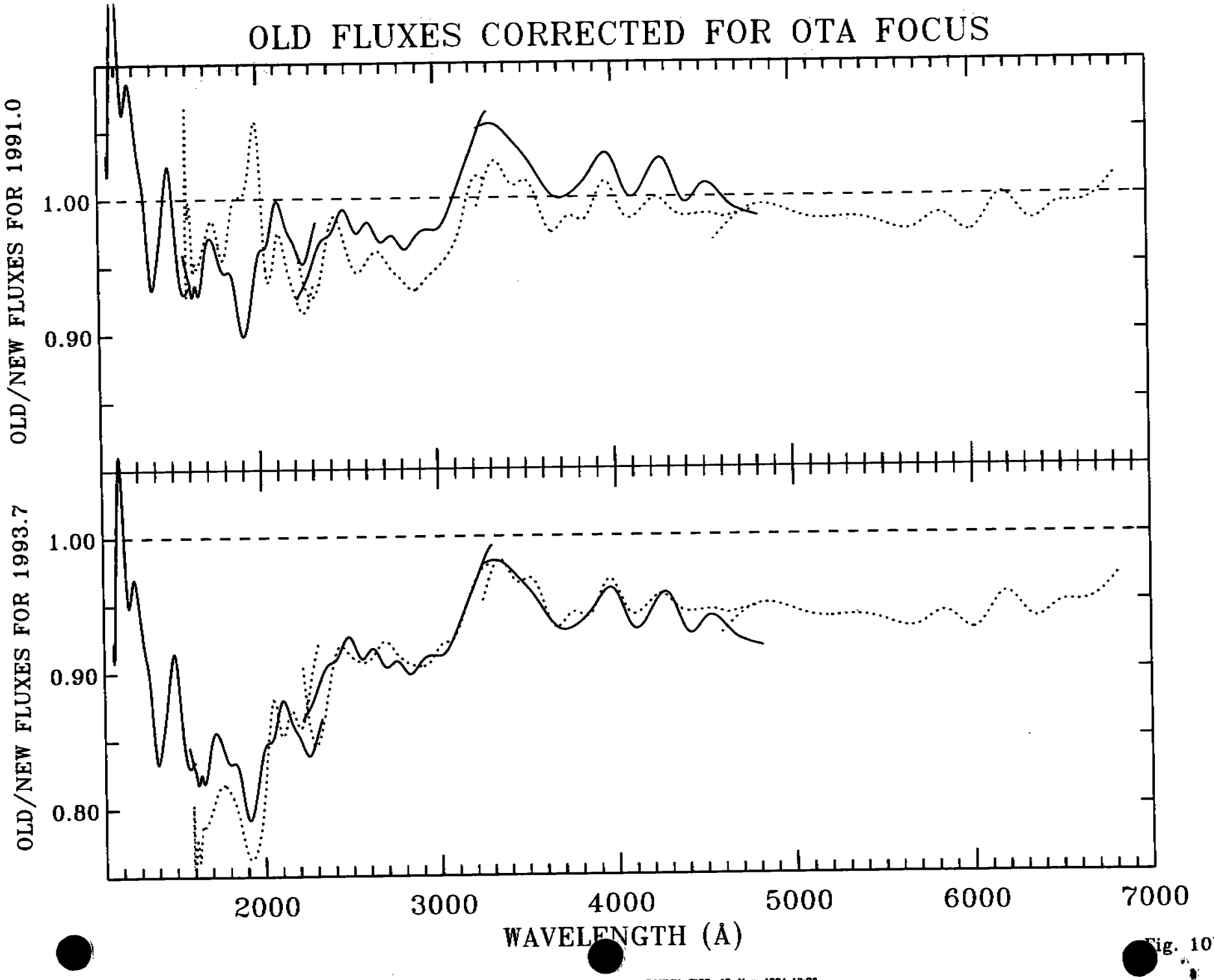
OLD FLUXES CORRECTED FOR OTA FOCUS
OLD/NEW FLUXES FOR 1991.0
1.00
0.90
OLD/NEW FLUXES FOR 1993.7
1.00
0.90
0.80
2000
3000
4000
5000
6000
7000
WAVELENGTH (Å)

Fig. 10b